Comparative analysis of vestibular ecomorphology in birds

Roger B. J. Benson[1*], Ethan Starmer-Jones[1*], Roger A. Close[2], Stig A. Walsh[3,4]

[1]*Department of Earth Sciences, University of Oxford, Oxford, United Kingdom*

[2]*School of Geography, Earth and Environmental Sciences, University of Birmingham, Edgbaston, Birmingham, United Kingdom*

[3]*Department of Natural Sciences, National Museums Scotland, Edinburgh, United Kingdom*

[4]*School of GeoSciences, The King's Buildings, Edinburgh, United Kingdom*

*joint first authors

Correspondence

Roger Benson, Department of Earth Sciences, University of Oxford, South Parks Road, Oxford OX1 3AN, United Kingdom. E: roger.benson@earth.ox.ac.uk

Abstract

The bony labyrinth of vertebrates houses the semicircular canals. These sense rotational accelerations of the head and play an essential role in gaze stabilisation during locomotion. The sizes and the shapes of the semicircular canals have hypothesised relationships to agility and locomotory modes in many groups, including birds, and a burgeoning paleontological literature seeks to make ecological interpretations from the morphology of the labyrinth in extinct species. Rigorous tests of form-function relationships for the vestibular system are required to support these interpretations. We test the hypothesis that the lengths, streamlines, and angles between the semicircular canals are related to body size, wing kinematics, and flying style in birds. To do this, we applied geometric morphometrics and multivariate phylogenetic comparative methods to a dataset of 64 three-dimensional reconstructions of the endosseous labyrinth obtained using µCT scanning of bird crania. A strong relationship between centroid size of the semicircular canals and body size indicates that larger birds have longer semicircular canals compared to their evolutionary relatives. Wing kinematics related to manoeuvrability (and quantified using the brachial index) explain a small additional portion of the variance in labyrinth size. We also find strong evidence for allometric shape change in the semicircular canals of birds, indicating that major aspects of the shape of the avian labyrinth are determined by spatial constraints. The avian braincase accommodates both a large brain, a large eye, and large semicircular canals compared to other tetrapods, and negative allometry of these structures means that the restriction of space within the braincase is intense in birds, and especially in small birds. This may explain our observation that the angles between planes of the semicircular canals of birds deviate more strongly from orthogonality than those of mammals, and especially from agile, gliding and flying mammals. Furthermore, we find little support for relationships between labyrinth shape and flying style or wing kinematics. Overall, our results suggest that the topological problem of fitting long semicircular canals into a spatially constrained braincase is more important in determining the shape of the avian labyrinth than the specifics of locomotory style or agility. Our results tentatively indicate a link between visual acuity and proportional size of the labyrinth among birds. This suggests that the large labyrinths of birds compared to other tetrapods may result from their generally high visual acuities, and not directly from their ability to fly. The endosseous labyrinths of extinct birds and their close dinosaurian relatives may allow broad inferences about flight or vision, but so far provide few specific insights into detailed aspects of locomotion.

Key words: endosseous labyrinth; semicircular canals; form-function relationships; paleoecology; phylogenetic signal; birds.

Introduction

The vertebrate vestibular system provides sensory information on head motion to the brain. These stimuli play a central role in stabilising the head during locomotion, and it is clear that some aspects of vestibular system morphology reflect the locomotory styles of species (e.g. the lengths, diameters and orientations of the semicircular canals; reviewed by Spoor & Zonneveld, 1998; Spoor, 2003; Sipla & Spoor, 2008; Walsh & Milner, 2011; Ekdale, 2016). This form-function relationship has been subject to significant quantitative investigation in mammals, primarily based on examination of the endosseous labyrinth (the bony fossa that houses the vestibular system; Spoor et al., 2007; Lebrun et al., 2010; Billet et al., 2012; Gunz et al., 2012; Alloing-Seguier et al., 2013; Malinzak et al., 2012; Berlin et al., 2013; Grohe et al., 2015; Pfaff et al., 2015). In contrast, there have been few quantitative studies of labyrinth morphology in other tetrapods (but see Smith & Clarke, 2012; Georgi et al., 2013; Yi & Norell, 2015; Azuma et al., 2016), or of general patterns of labyrinth evolution and their relationships with ecology across tetrapods as a whole. As well as having significance for functional biology, these relationships have importance for the field of palaeobiology, because they can be used to constrain hypotheses of the ecologies of extinct species (e.g. Spoor et al., 2002; Witmer et al., 2003; Domínguez et al., 2004; Georgi et al., 2013; Yi & Norell, 2015).

Extant birds display a wide range of flight styles and abilities, and the co-ordination of flight depends extensively on vestibular stimuli (Walsh et al., 2013). Birds have large semicircular canals compared to other tetrapods (Jones & Spells, 1963), and compared to their flightless relatives (the non-avian dinosaurs; e.g. Domínguez et al., 2004; Witmer et al., 2009). This may be an adaptation to flight. Integrated information from the optic flow field and vestibular system is crucial for maintaining dynamic balance within a three-axis reference system (Wylie & Frost, 1999; and e.g. Bhagavtula et al., 2011; Goller & Altshuler, 2014; for optic flow field), and retinal gaze stabilisation is a prerequisite for this. Gaze stabilisation allows individuals to maintain visual targets in focus at fixed points on the retina during locomotion. Stabilisation is achieved through two reflexes, the vestibulo-ocular reflex (VOR) and vestibulo-collic reflex (VCR), operating on the extraocular and cervical musculature respectively (Bilo & Bilo, 1978; Wilson & Melville-Jones, 1979; Leigh & Brandt, 1993; Spoor, 2003; Warrick et al., 2002). These result in compensatory movements of the eyes and neck in the opposite sense to head motions, avoiding blurred vision during locomotion. This may be especially important for taxa that rely upon visual clues to navigate cluttered environments such as forest canopies. Furthermore, well-developed gaze stabilisation is thought to be essential in birds with unstable (e.g. hovering) flight and for complex, fast aerial manoeuvres involved in nuptial displays and pursuit of flying prey (Walsh et al., 2013; Dakin et al., 2016).

Despite its obvious importance, the relationship between flying style and vestibular morphology in birds remains poorly constrained. This relationship has relevance to the evolutionary origin of bird flight, which is of significant interest in vertebrate palaeobiology (e.g. Gauthier & Padian, 1985; Padian & Chiappe, 1998; Dial, 2003; Xu et al., 2003; Longrich et al., 2012; Foth et al., 2014). Progress on the origins of avian flight has been stimulated by discoveries of numerous bird-like dinosaur fossils with preserved feathers (e.g. Xu et al., 2003; Xu et al., 2014; Xu et al., 2015). So far, palaeoecological inferences on the flight abilities of fossil birds have been attempted based on wing morphologies (e.g. wing loading, aspect ratio) furcula morphology, and the morphology of the forelimb skeleton (Viscor & Fuster, 1987; Simons, 2010; Close & Rayfield, 2012; Sievwright & MacLeod, 2012; Taylor, 2014). With further study, the labyrinth might provide additional insights into avian palaeoecology.

The labyrinths of bird-like stem-group taxa such as *Archaeopteryx* (Jurassic) and *Fukuivenator* (Cretaceous) provide evidence of the evolutionary origins of avian vestibular morphology by comparison with modern taxa, alongside other fossils (Domínguez et al., 2004; Azuma et al., 2016). Based on this evidence, the series of acquisition of bird-like features of the labyrinth is broadly understood (e.g., overall enlargement of semicircular canal radii, extension of the anterior canal posteriorly and posterior canal ventrally, posterodorsal tilting of the crus communis, enlargement of the ampullae; Witmer et al., 2008). However, the absence of a quantitative framework for interpreting labyrinth morphology has prevented strict interpretations of the ecological significance of observed labyrinth morphologies.

Semicircular canals detect angular (i.e. rotational) accelerations of the head in three spatial planes, and reviews of their function have been provided by Spoor & Zonneveld (1998), Spoor (2003), Sipla & Spoor (2008), Walsh & Milner (2011) and Ekdale (2016) among others. Sensitivity to head movement has been attributed to various aspects of semicircular duct morphology, including arc length (Spoor et al., 2007; Georgi et al., 2013). Longer semicircular canal arcs should be more sensitive to rotation (Jones & Spells 1963; Ten Kate, 1969; Muller, 1994; Hullar, 2006), and some comparative evidence of this relationship comes from the observation that agile mammals, including many arboreal taxa, with fast, jerky locomotion requiring a well-developed vestibular function, have proportionally longer canals (relative to body mass) than cautious, sluggish mammals (Spoor et al., 2007; Billet et al., 2012). This relationship has been used to infer agility in extinct primates (Silcox et al., 2009), but is redundant with a multivariate relationship between body mass, visual acuity and eye size. This multivariate relationship suggests that more agile mammals require greater visual acuity, and therefore more effective gaze stabilisation, which is provided by the presence of proportionally longer semicircular canals (Kemp & Kirk, 2014). A relationship between canal lengths and aerial manoeuvrability has been proposed in birds (Hadžiselimović & Savković, 1964). If such a relationship exists then semicircular canal lengths should be positively correlated with the degree of acrobatic locomotion in which a bird species routinely engages.

The angles between the best-fit planes of the semicircular canals may have even greater functional significance than their lengths for predicting agility. Malinzak et al. (2012) investigated the variance in sensitivity of the canal system to rotations in different planes, which can be approximated by the variance from 90° of the angles between the major planes of the canals (Malinzak et al., 2012; Berlin et al., 2013), finding that primates with faster head rotations had lower variance in sensitivity among angles. This strong, size-independent relationship has important implications for understanding how the labyrinth functions, and also for palaeoecological inference. However, it has not been investigated in birds, presenting a knowledge gap that impedes our understanding of the evolution of somatosensory capacity in vertebrates.

Here, we use X-ray micro-CT (µCT) scanning and 3D geometric morphometrics to investigate the influence of locomotion on avian semicircular canal morphology. Our objective was to identify statistically significant form-function relationships between flight styles and both the size and shape of the semicircular canals in extant birds. These predictive relationships may form a crucial but largely unexplored cornerstone of avian palaeoecology, and promise to allow probabilistic determinations of ecologies of extinct animals known only from fossils.

Information about vestibular morphology in extinct species comes mostly from fossils, in which only the bony anatomy is preserved. In life, endosseous canals housed the membranous portions of the vestibular system, which are not preserved in fossils (e.g. Walsh et al., 2014). Therefore, the endosseous space forms the basic data available to palaeoecological study. Since it is also difficult to study the membranous labyrinth directly in extant animals (Spoor, 2003), most recent studies of extant species have also focussed on the endosseous semicircular canals. These provide reliable information on key aspects of the mean endolymph flow paths (David et al., 2010): their arc lengths, and their courses, or streamlines (including the topologies of individual canals, and the angles between them). Other factors, such as the diameters (=calibres) of the membranous canals, are difficult to infer from the endosseous labyrinth as the thickness of the membranous canals can vary both intra- and inter-specifically (David et al., 2016). Although canal diameters are likely to affect the sensitivity of vestibular afferents (Rabbitt et al., 2004), they have yet to be investigated across vertebrates or even within a single clade. This is an obvious target for future study. Nevertheless, the endosseous labyrinth provides information on other aspects of the vestibular morphology, and has become accepted as an adequate proxy for soft-tissue morphology until further comparative anatomical work is conducted (Walsh et al., 2009, 2014; Alloing-Seguier et al., 2013; Grohe et al., 2015; David et al., 2016).

Materials and Methods

Morphometric Dataset Assembly. This study uses µCT scans of 64 avian crania assembled by S.W. (extended from Walsh et al., 2009, 2013) from the Natural History Museum, London (NHM) and National Museums Scotland, Edinburgh (NMS). Crania were scanned using Nikon Metrology HMX ST CT scanners (at the University of Abertay, NHM and Nikon Metrology, Tring) (see Walsh et al., 2009, 2013 for further scan methodology). The species sampled represent 51 families and 24 orders (Table 1) selected to represent a wide range of habitats and ecologies, with flight styles ranging from flightless to highly agile dynamic fliers. This dataset should therefore capture a large proportion of the ecomorphological variation of the bird labyrinth. Our morphometric data and flight style scores are available in the Supplementary Information. Our CT data and 3D labyrinth models are provided on Dryad (link on acceptance), along with landmark data, principal component analysis scores, taxon data (e.g. body mass, flying style categorisation), and phylogenetic trees used for statistical comparative analysis.

We segmented the left endosseous labyrinth from the µCT scan of each bird cranium using the semi-automated *Livewire* tool of Materialise Mimics 16.0 (Materialise NV, Belgium), applying specimen-specific thresholds to ensure bone was excluded from the labyrinth model. Each of the semicircular canals (anterior [= rostral], posterior [=caudal], and lateral [=horizontal]; Fig. 1B) was isolated from the labyrinth using a 3D mask-editing tool, resulting in four separate 3D voxel models (Fig. 2A). The use of separate models for each semicircular canal was essential for the study of bird labyrinths, in which the canals intersect each other, making it difficult to extract accurate canal midline skeletons (Fig. 2B, and described below) for landmarking when the entire labyrinth model is used.

The voxel models were imported into Avizo 8.0 (FEI Visualization Sciences Group, Berlin, Germany). The *autoskeleton* function of Avizo was used to create a smoothed midline skeleton by iteratively thinning each of the semicircular canals until a single line of voxels remained (Fig. 2B). This procedure was conducted using 1000 iterations, with a ‘smooth’ coefficient of 0.99, and ‘attach to data’ parameters set of values between 0.2-0.6 based on inspection of the resulting midline skeletons. This central ‘streamline’ represents the mean endolymph flow path (David et al. 2010). The *autoskeleton* algorithm sometimes results in small kinks in the reconstructed canal streamlines (e.g. anterior semicircular canal in Fig. 2B–C). The effect of these was entirely negated by downsampling of each semilandmark series to 12 semilandmarks (see below).

We placed six conventional landmarks on the midline skeletons of the semicircular canals of each specimen (Fig. 2C: numbered 1–6). These were placed where the slender portions of the canals intersect their respective ampulla, where the posterior semicircular canal (PSC) and anterior semicircular canals (ASC) intersect the crus communis, and where the lateral semicircular canal (LSC) intersects the vestibule. Conventional (or 'traditional') landmarks represent biologically and geometrically homologous points that are reliably and repeatably locatable in every specimen (Gunz & Mitteroecker, 2013). This criterion is essential for ensuring statistical analyses are biologically interpretable and meaningful. Our landmarking scheme is a simplified version of that used by Gunz et al. (2012). We reduced the number of landmarks because our study aimed only to address the question of how the total size and the courses of the semicircular canals vary in respect to flying style, wing kinematics and body size. Furthermore, we were not able to consistently calculate accurate midlines for the vestibule, ampullae and common crus, so fixed landmarks could not be placed within these structures.

Conventional landmarks alone are insufficient to capture the shapes of smoothly curving midline skeletons that lack repeatably locatable points along their length (Gunz et al., 2012; Gunz & Mitteroecker, 2013). Therefore, we also placed semilandmarks along the midline skeleton of each canal, traversing from the ampullary to the non-ampullary end (Fig. 2C). More landmarks were placed on longer canals, and the number of landmarks per canal ranged from 21 to 150. Landmarks were subsequently resampled to an equal number of 10 equally spaced sliding semilandmarks per canal (plus their fixed start and end points, resulting in 12 landmarks per curve in total) using the digit.curves() function of the version 3.1.1 (Adams & Otarola-Castillo, 2013) package of R 3.2.1 (R Core Team, 2015). This number was selected because larger numbers resulted in sliding errors for some taxa during generalised Procrustes superposition. In addition to their use for geometric morphometrics (described below), we also used eigenvector analysis of these landmarks to calculate the best fit plane of each semicircular canal, and the angles between these planes. These were used to test the hypothesis that the inter-plane angles of the semicircular canals of birds have a relationship to flying style or other factors.

Flight Classification and Other Variables. Studies of the relationship between avian skeletal morphology and flying style have classified flight modes using various methods. Typical approaches have characterised flight modes using mutually exclusive flight categories that are intended to capture the predominant flying style of each taxon (e.g. Rayner, 1988; Norberg, 1990; Wang et al., 2011). Pennycuick (2008) outlined a scheme consisting of four fundamental flight styles: soaring, continuous flapping, flap-gliding and intermittent bounding. This was later modified in subsequent studies to include more categories (Table 2; Bruderer et al., 2010; Close & Rayfield, 2012).

These schemes are difficult to apply because most birds are capable of multiple different flight modes, and some flight modes are nested within more generalised flight modes. For example, dynamic soaring (soaring using the intersections of air currents) and static soaring (soaring using thermals; or classic ‘soaring’) are both types of soaring flight that require little energy expenditure to stay airborne. Typically, the flight mode perceived as being most frequently used by each bird is recorded. However, this introduces subjectivity, because the flight modes of individual birds are influenced by ethology, physiological condition, and the dependence of flight mode on the environment (e.g. soaring capabilities are reliant on the presence of thermal airflows or strong airflow gradients; flapping may be necessary close to the ground and in closed environments) (Viscor & Fuster, 1987). Furthermore, some flight behaviours might be more important than others, even if they are not the predominant flight style. Risky modes of locomotion are under greater selective pressures, and could therefore impose strong constraints on labyrinth morphology, even when they are used only infrequently (Malizak et al. 2012). Therefore, categorisations of the type shown in Table 2 are subjective, and the assignment of a single taxon can vary between researchers. For example, *Larus argentatus* (European Herring Gull) has been assigned both continuous flapping (Bruderer et al., 2010) and soaring as main flight modes (Viscor & Fuster, 1987).

To capture the complexities and plasticity of the flight behaviours of each species, we therefore modified a classification scheme developed by Taylor (2014). Nine ecological characters were scored as either present (1) or absent (0) for each taxon: pelagic (dynamic) soaring, soaring over land, submerged aquatic feeding, sally hunting, pursuit hunting, use of cluttered airspace, flightless, burst-adapted flight, and flap-bounding (flap-bounding was not included by Taylor [2014]; and two of Taylor's categories were removed because they are not relevant to flight dynamics: use of migration and commuting to feed young). Full definitions are given in Appendix S1. Following Taylor (2014), we scored any (even slight) indication of the use of a flight mode as presence (1). It is not currently possible to determine the proportion of time or energy that individuals of a species spend on each flight mode, although this may be desirable.

Our scheme allows multiple flight behaviours to be assigned to each species. This approach emphasises the range of behaviours that each species is known to be capable of performing. We obtained relevant ecological information from the multi-volume “Handbook of the Birds of the World” (del Hoyo et al., 1992, 1994, 1996, 1997, 1999, 2001, 2002, 2005, 2006, 2008, 2009, 2010), combining information on individual species, with information from higher taxa (where species-level information was insufficient) and observations of natural history videos (primarily from http://www.hbw.com/ibc and http://www.arkive.org/). Body mass (or the mean body mass when a range was given) was also recorded from this handbook series.

This scheme uses categories closely-related to (1) aerial manoeuvrability, ranging from static soaring to more dynamic pursuit hunting taxa, and (2) mode of locomotion (aerial, subaqueous, and flightless), which is expected to influence labyrinth morphology (e.g. Thewissen & Nummela, 2008 for adaptation of the labyrinth to subaqueous locomotion). It is thus relevant to determining form-function relationships of the labyrinth. Additionally, it recognises multiple ecological factors that could influence canal morphology: steady flight, hunting on the wing, and interacting with the environment. This contrasts with the categorisation scheme used by Close & Rayfield (2012; Table 2), which focuses on capturing visual differences that result from differing wing kinematics between flight modes in steady, level flight.

Wing shape and area, along with body mass, are among the variables that determine the physical flight envelope of birds (Pennycuick, 2008). Although the wing chord is largely determined by the composition of remiges, the relative lengths of the wing bones, such as the humerus and ulna, are a basic component of wing shape. The ratio of humerus length to ulnar length, or ‘Brachial Index’ (BI; Nudds et al., 2007), is readily obtained from extant birds and can frequently also be measured in fossil specimens. Taxa that use high amplitude flapping flight (e.g. swifts, passerines, hummingbirds) tend to have lower BI values (<0.7; i.e., a relatively shorter humerus) than less manoeuvrable taxa such as soaring birds, subaqueous fliers (1.1-1.4; i.e., a relatively longer humerus) and flightless taxa (>1.3; Nudds et al., 2007). Since BI values are directly related to flying capability, we used BI as a continuous-valued skeletal proxy for aerial manoeuvrability. Values of brachial index were obtained from Nudds et al. (2007) and Walsh et al. (2013). Because these values can be directly measured, rather than subjectively scored, and since aerial agility in birds is difficult to quantify directly, we considered them as being preferable for quantitative analyses to the categorical agility ranks such as that devised for mammals by Spoor et al. (2007).

Geometric Morphometric Analysis. Geometric morphometric analyses were performed in R version 3.2.1 (R Core Team, 2015) using the packages geomorph 3.1.1 (Adams & Otarola-Castillo, 2013) and Morpho 2.3.0 (Schlager, 2016). First, a generalised Procrustes analysis (GPA; Gower, 1975) was performed on our set of six landmarks and 30 semilandmarks. GPA optimally superimposes landmark configurations by removing the effects of position, size and orientation (Gower, 1975; Rohlf & Slice, 1990). When semilandmarks are used, GPA additionally permits ‘sliding’ of those semilandmarks along the tangent directions defined by adjacent semilandmarks (and in this case along three separate curves representing the three semicircular canals) to minimise the TPS bending energy between the reference and target configurations. This is done because the initially arbitrary equal spacing of semilandmarks may not be the optimal configuration (Bookstein, 1997; Gunz et al., 2005; Webster & Sheets, 2010; Gunz & Mitteroecker, 2013). Variation remaining among the landmark constellations of specimens following GPA is independent of the initial positions, sizes and orientations of landmark constellations, and therefore represents only the shape differences between taxa (Kendall, 1977). Points are then projected into a linear Euclidean tangent space that intersects the Procrustes shape space at the mean shape. This allows application of linear algebraic tools such as principal components analysis (PCA), which we subsequently used to quantify the major axes of shape variation among specimens.

The centroid size of each labyrinth's original landmark/semilandmark configuration is the square root of the sum of squared distances between each landmark and the configuration's centroid (e.g. Webster & Sheets, 2010). The value is output from GPA and was used as a measure of the total size of the combined system of semicircular canals. Unlike the canal radius of curvature, a commonly used size metric that only utilises distances between extreme landmarks (e.g. Spoor et al., 2007) centroid size has the favourable attribute of weighting each landmark equally to obtain a measure of average radius. Note however that centroid size only approximates the radius of curvature, and does so most effectively when interspecific differences in the angles between the planes of the semicircular canals are minimal (because canals with the same radii of curvature will have different centroid sizes as the angles change).

Statistical Hypothesis Tests. We used two approaches for testing the relationships of labyrinth shape, size, and the angles between the planes of the semicircular canals (henceforth: inter-canal angles) with other variables: phylogenetic generalised least squares regression (Grafen, 1989) and two-block partial least squares (Rohlf & Corti, 2000). All analyses were conducted using the R packages nlme 3.1-120 (Pinheiro et al., 2015), ape 3.4 (Paradis et al., 2004), and geomorph 3.1.1 (Adams & Otarola-Castillo, 2013).

Regression analyses were used to test the following relationships and hypotheses using species-specific data:

(1) The relationships between the scores for individual principal component axes, representing major aspects of labyrinth shape variation, and $\log_{10}$-transformed body mass. This tests the hypothesis that one or more of the major axes of labyrinth shape change among birds represents allometry.

(2) The relationships between the principal component scores and log-transformed brachial index (BI). This tests whether specific modes of labyrinth shape variation correspond to differences in aerial manoeuvrability among bird species.

(3) The relationships of both $\log_{10}$-transformed labyrinth centroid size and inter-canal angles with $\log_{10}$-transformed body mass, $\log_{10}$-transformed brachial index, or both (in multiple regressions). This tests the hypotheses that labyrinth size and orthogonality scale with body mass and/or aerial manoeuvrability in birds (Hadžiselimović & Savković, 1964; Malinzak et al. 2012).

Phylogenetic generalised least squares regression (pGLS; Grafen, 1989) uses the covariances expected among taxa given a phylogenetic tree to modify the assumptions of leas squares regression. When Brownian motion (Felsenstein, 1985) is assumed, pGLS is mathematically analogous to ordinary least squares regression of phylogenetic independent contrasts (Garland & Ives, 2001). This represents a model in which strong phylogenetic signal is present in a relationship of interest due to evolution along lineages. This causes the intercept of the relationship between variables to evolve at a constant, non-directional rate on the phylogeny. Pagel's λ (Pagel, 1999) is a parameter that scales the strength of phylogenetic signal between the inferred phylogeny with its branch lengths (λ = 1), and a star phylogeny in which all taxa effectively represent independent observations (λ = 0; for ultrametric trees).

Although strong phylogenetic signal is often assumed by comparative studies of trait data, form/function relationships can be strongly constrained by the physical laws of the universe, and when this occurs phylogenetic signal is expected to be zero (λ = 0) (Motani & Schmitz, 2011). Therefore, we used pGLS with a freely varying λ parameter, optimised using maximum likelihood to quantify the role of phylogeny in the relationships between explanatory and dependent variables. This model was also used by Berlin et al. (2013) to test the relationships of vestibular sensitivity with deviation from orthogonality, deviation from left-right angle symmetry, and deviation from left-right coplanarity. For the purpose of this model fit, we sampled 100 phylogenies from the tree distribution of Jetz et al. (2012: birdtree.org) and conducted all analyses across the full set of phylogenies. The analyses presented in this paper result from the Ericson et al. (2006) backbone. However, analyses using the Hackett et al. (2008) backbone yielded essentially identical results. This provides a test of whether results are sensitive to uncertainty in the specific phylogenetic topology. We also used Akaike's information criterion for small sample sizes (AICc; Sugiura, 1978; Burnham & Anderson, 2004) to choose among combinations of explanatory variable(s) for each dependent variable. Conceptually, the use of AICc allows the 'assumptions' of specific statistical/evolutionary models, to be tested by explicitly comparing these models to each other. This allows estimation, rather than assumption, of the nature of the co-evolutionary relationships between variables.

We used two-block partial least-squares regression (2B-PLS; Rohlf & Corti, 2000) to quantitatively assess the relationship between our multivariate set of flight characters (see flight classification, described above) and multivariate labyrinth shape represented by our principal component axes. We analysed the principal component axes, rather than the procrustes-aligned co-ordinates (e.g. Zelditch et al., 2012) because we found it useful to test the effects of excluding the first principal component axis (PC1), which represents allometric variation (see Results). Two-block partial least squares analysis can be used to determine the structure of covariance between two multivariate datasets, and has the desirable property of considering the effects of all flight characters simultaneously. This is crucial in our dataset where flight characters are non-exclusive and frequently co-occur. 2B-PLS requires continuous-valued multivariate inputs. Therefore we transformed our categorical (presence/absence) flying style data to a set of seven continuous valued composite variables using principal co-ordinates analysis of the pairwise Gower distances among species prior to 2B-PLS analyses.

In contrast to least-squares regression, 2B-PLS treats the two sets of variables symmetrically – so no causal relationship is assumed. Pairs of latent variables, or composite axes, are constructed from linear combinations of the original variables (analogous to principal component axes). Each pair of latent variables corresponds to a ‘dimension’ that maximises the covariance between the two multivariate datasets (Rohlf & Corti, 2000). Covariance and correlation coefficients of latent variables were subsequently calculated and their statistical significance was evaluated using permutation tests in geomorph. Any statistically significant dimensions were interpreted by contrasting the relevant loading coefficients (**F_1** and **F_2**). Because we analysed comparative data, which may contain phylogenetic signal, we applied phylogenetic 2B-PLS (Adams & Felice, 2014). Ordinary (non-phylogenetic) 2B-PLS was also applied for comparison. Unlike the situation with regression analyses, a model comparison framework is not yet available for 2B-PLS, so we were not able to determine whether ordinary or phylogenetic 2B-PLS was most appropriate given the data. Nevertheless, these analyses can be seen as asking two separate questions: (1) Ordinary 2B-PLS: do the labyrinth morphologies observed among a sample of extant birds correlate to the flight styles of those birds (a correlation that may be caused by independent evolution of these traits on the branches of the same phylogeny)? (2) Phylogenetic 2B-PLS: do evolutionary changes in bird labyrinth shape correlate with evolutionary changes in flight style reconstructed on the branches of a phylogeny, consistent with the occurrence of linked evolution due to a form-function relationship?

Results

Labyrinth centroid size. Across all the flying and flightless birds in our sample, labyrinth size is best explained by body mass and brachial index together (Fig. 3A; Table 3, upper portion; this was true across all 100 phylogenies), according to AICc. The best model of the relationships among these variables is one in which phylogenetic signal (λ) is allowed to vary during model fitting. The Pagel's lambda (λ) value of 0.74 (range from 0.66 to 0.80) estimated across all phylogenies indicates an intermediate amount of phylogenetic signal in the relationship between labyrinth size, body mass and brachial index (Table 3). A low, positive coefficient of body mass (0.20 for all phylogenies; Table 3) indicates negative allometry of labyrinth size with body mass. Despite the low value of this coefficient, variation in body mass explains a large portion of the size variance measured in bird labyrinths ($R^2 = 0.78$ in bivariate ordinary least squares regression; Table 3). Brachial index is not correlated with labyrinth size in bivariate regressions (Fig. 3B; Table 3), but has a significant negative correlation when variation in body mass is taken into account using multiple regression (Table 3; $p = 0.001$ or less for all phylogenies; Fig. 3C). Birds with higher values of BI therefore have proportionally larger labyrinths relative to their body masses. Nevertheless, the explanatory power of labyrinth centroid size to predict brachial index is relatively low once the effects of body mass are excluded: multiple regression models of brachial index on body mass and centroid size have R^2 of between 0.038 and 0.169 (across 100 phylogenetic topologies; median $R^2 = 0.125$) (Table 4).

Flightless birds have proportionally small labyrinths and extremely high values of BI (e.g. Fig. 3). They may therefore drive the relationship of BI with labyrinth size. When data only for flightless birds are analysed, statistically significant coefficients similar to those found in the previous analysis are found for body mass and BI (Table 3, lower portion). Nevertheless, the AICc weight of a model explaining labyrinth centroid size using body mass and brachial index is lower than that of a model explaining labyrinth centroid size using only body mass (although both have non-negligible AICc weights, rendering model choice equivocal; Table 3). Overall, therefore, we find that brachial index, our proxy for wing kinematics, explains only a small portion of the variance in labyrinth size.

Labyrinth inter-canal angles. The angles between the best-fit planes of pairs of semicircular canals in birds are typically greater than 90° (Fig. 4: 1.57 radians, indicated by dashed grey line). The median angles are 94.0° (1.64 radians) between the anterior and lateral canals, 98.0° (= 1.71 radians) between the anterior and posterior canals, and 93.0° (= 1.62 radians) between the lateral and posterior canals. These are substantially greater than the mean angles reported in mammals by Berlin et al. (2013: 84.5°, 91.9°, and 90.3° respectively), but have similar standard deviations. Variation in the angle between the lateral and posterior semicircular canals of birds (Fig. 4B: standard deviation = 4.4°) is less than variation in the angle between the other two combinations of pairs of canal (standard deviation = 7.3° [anterior and lateral canals] and 8.1° [anterior and posterior canals]). No clusters are evident by visual appraisal of the distribution of flight modes with respect to inter-canal angles (Fig. 4), and statistical evidence of clustering is tested further by our two-block partial least squares analyses (below), because principal component axes (especially PC1 and PC2, described below) capture major variations in inter-canal angles well.

Neither the absolute values of inter-canal angles nor their positivised deviations from 90° show any statistically significant relationship with either brachial index or body mass for the angles between the anterior and posterior canals or posterior and lateral canals (Fig. 4; Tables S1–S3). The angle between the anterior and lateral semicircular canals has a significant positive relationship with body mass (Fig. 4A; Table S1), and the positivised deviation of this angle from 90° has a statistically significant positive relationship with brachial index (Table S1; range of p-values across all phylogenies from 0.007 to 0.032). The relationship of the absolute angle between the anterior and lateral semicircular canals with body mass explains an R^2 of 0.073 to 0.265 among phylogenies (median R^2 = 0.148) (Table S1). The relationship of the absolute deviation from 90° with brachial index explains a much smaller amount of variance, from 0.038 to 0.113 among phylogenies (median R^2 = 0.052) (Table S2).

Labyrinth shape—principal components analysis (PCA). The first three principal components collectively summarise more than 65% of the variance in labyrinth shape in our dataset (Table 5). The first principal component axis (PC1) contains a strong allometric signal (see below; Table 6), and each subsequent principal component axis up to the eighth (PC2–PC8) explains at least 5% of the non-allometric shape variance (after excluding PC1; Table 5). Detailed descriptions of the shape changes on PC1–PC3 are given here and visualised in Figures 5–7. Movies showing deformations along PC1–PC12 are available from Dryad (link on acceptance).

PC1 describes displacement of the anterior vertical canal (ASC) from anterior (negative values) to posterior (positive values), accompanied by some reduction of its diameter at positive values (the anterior ampulla and common crus become closer together). The lateral canal (LSC) is longer, and therefore extends further anteriorly, laterally and posteriorly at positive values of PC1, and is shorter and more recessed at negative values of PC1. Furthermore, the plane of the lateral canal slopes ventrolaterally relative to the plane of the anterior canal at negative values of PC1 (at the minimum value of PC1, the angle between the planes equals 102°, or 1.78 radians), but can be orthogonal to the anterior canal at positive values of PC1 (angle = 84°, or 1.47 radians). Variation in the inter-canal angles for other pairs of semicircular canals is negligible along PC1. Both the LSC and posterior vertical canal (PSC) become tilted anteriorly at positive values of PC1. The PSC becomes shorter by reduction of its ventral portion at positive values of PC1, and longer with a more extensive ventral portion at negative values of PC1.

PC2 describes reduction of the anteroposterior spans of both the ASC and LSC at positive values, causing a reduction in radius of curvature. An increase in the anteroposterior spans of these canals is evident at negative values of PC2, causing increases in radius of curvature. Changes in the span of the ASC along PC2 are anteroposteriorly symmetrical, whereas changes in the span of the LSC result predominantly from changes to its posterior extent. Negative values of PC2 correspond to a more sinuous ASC when seen in dorsal view, and positive values correspond to a more planar configuration of the ASC. Negative values of PC2 correspond to a more dorsal position for the LSC and positive values correspond to a more ventral position. Positive values of PC2 describe an increase in the height of the common crus, so that the posterior end of the ASC then enters the common crus at a more anterodorsally inclined angle. Unlike the other two canals, the PSC shows little change along PC2. However, the angle between the planes of the anterior and posterior canals is high at negative values of PC2 (angle = 105°, or 1.85 radians for the minimum value of PC2) and can be orthogonal at positive values (angle = 87.7°, or 1.53 radians for the maximum value of PC2). Variation in the inter-canal angles for other pairs of semicircular canals is negligible along PC2.

PC3 describes increase in the relative height of the ASC at positive values, and decrease in the height of the ASC at negative values. These changes correspond to changes in the relative length of the ASC, with a proportionally larger ASC, and smaller LSC and PSC (see below), occurring at positive values of PC3. Positive values of PC3 also correspond to lateral deflection of the anterior portion of the ASC. PC3 also describes changes in the relative size of the LSC, with a smaller, dorsolaterally tilted LSC occurring at positive values, and a larger, ventrolaterally tilted LSC occurring at negative values. This results in variation of the angle between the planes of the anterior and lateral semicircular canals between the minimum value of PC3 (angle = 96.5°, or 1.69 radians) and maximum value of PC3 (angle =

88.7°, or 1.55 radians). The angle between the planes of the anterior and posterior canals also varies negatively with PC3 score (between 100.4°, or 1.75 radians, and 95.7°, or 1.67 radians). Positive values of PC3 describe a mediolaterally narrower PSC (i.e. does not extend as far medially).

The ordination of species into a morphospace defined by PC1–PC3 does not show any striking patterns of labyrinth morphology with respect to coarse flight categories (Fig. 7; flightless, burst-adapted, pursuit hunting). This does not exclude the possibility of a relationship with other flying styles. Neither does it preclude the possibility of a complex relationship in which phylogeny determines the basic structure of the labyrinth that is then modified consistently by evolutionary changes in flying style, or of a situation in which other PC axes explain less shape variance than PC1–PC3 but correspond more closely to flight ability. These possibilities are tested by our 2B-PLS analyses, described below.

The results of bivariate and multiple linear regressions of the scores along individual principal components against body mass and brachial index are summarised in Tables 6–8 (PC1–PC3) and in the Supplementary Information (PC4–PC8; Tables S4–S8). The scores of the first principal component axis (PC1) correlate significantly with body mass (Fig. 8A, Table 6). Therefore, PC1 describes allometric shape variation. This correlation is negative, and explains and R^2 of 0.31 (Table 5). The presence of strong phylogenetic signal (λ) in the best regression models indicates that closely related taxa generally have similar labyrinths, but that phylogenetically-determined morphologies are then modified by allometric effects, with larger-bodied taxa having more negative values of PC1 (shape changes described above and shown in Fig. 5). Other principal component axes are not related to body mass (Tables 6–8 and Tables S4–S8 in the Supplementary Information). Although PC4 and PC8 show significant (PC8: p = 0.010; Table S8) or marginally non-significant (PC4: p = 0.058; Table S4) correlations, relationships with body mass for these variables are worse than an intercept-only null model and therefore have negative R^2 values (Tables S4, S8).

All principal component axes show either a weak or no relationship with brachial index. PC5 is the only principal component to correlate with brachial index at 95% significance (coefficient = -0.118; R^2 = 0.005; p = 0.0424; Table S5). This suggests that more positive PC5 scores correspond to taxa with smaller brachial indices and thus greater aerial manoeuvrability. However, the negligible generalised R^2 value of this model (= 0.01; Table S5) indicates that it is little better than an intercept-only null model and has negligible explanatory power.

Labyrinth shape—relationship with multivariate flight style. Both ordinary (non-phylogenetic) and phylogenetic two-block partial least-squares (2B –PLS) analyses indicate a significant multivariate association between labyrinth shape and the principal coordinates ordination of our flight categories. The association found by ordinary 2B-PLS has an R^2 of 0.70, and the association found by phylogenetic 2B-PLS has a median R^2 of 0.59 across all trees (Fig. S1).

Dimension 1 of our ordinary 2B-PLS analysis explains 86.5% of the total variance explained by the association, indicating that other dimensions explain only a small amount of variance. The loadings of dimension 1 indicate a relationship between our principal component axis 1 (PC1: allometry of labyrinth shape) and the first axis of our principal coordinates analysis (PCo1) (Table 9). PCo 1 separates taxa that engage in sally hunting, intermittent bounding and use of cluttered airspace from flightless taxa, and taxa that engage in pelagic soaring and submerged aquatic feeding (Fig. 9). It is likely that the correspondence between PCo1 and PC1 highlighted by ordinary 2B-PLS results from size-dependency of both axes.

Dimension 1 of our phylogenetic 2B-PLS analysis explains a median of 50.3% of the total variance explained by the association across all trees, dimension 2 explains 35%, dimension 3 explains 7.3% and subsequent dimensions explain even less. We therefore restrict our discussion to dimensions 1 and 2. Interpretation of these dimensions is complicated because of variation among analyses on different trees as to which principal components and principal coordinates axes contribute to the association on each dimension. Nevertheless, inspection of the median absolute loadings along these dimensions indicates that PC1, PC6, PC7, and PC11 contribute substantially to the multivariate association (Table 10).

To visualise the effects of the non-allometric shape changes involved in this non-allometric shape association (i.e. PC6, PC7, PC11), we conducted a second set of phylogenetic 2B-PLS analyses, excluding PC1. Dimension 1 of this analysis explains between 49.3% and 97.9% of the total variance explained by the analysis (median of total variance = 67.5%; ranging from 57.6% to 85.6% among phylogenies) (Fig. S2). Results for subsequent dimensions account for much less variance (median = 14.2% for dimension 2), and their vectors are less consistent among phylogenies. These are not discussed further here.

Across all phylogenies, the most important shape variables for dimension 1 of our non-allometric phylogenetic 2B-PLS analysis are PC11, which takes large positive values, and PC6 and PC7, which take large negative values. Collectively, these axes explain 10.0% of shape variation or 17.1% of non-allometric shape variation (Table 5). The second axis of our principal coordinates analysis (PCo2) is consistently the most important flight variable, taking large positive values that far exceed the magnitudes of any other PCo axes. An example for tree 1 is given in Table 11, but this result is consistent across all phylogenies that recover a significant phylogenetic 2B-PLS result. PCo2 separates birds that are capable of pursuit hunting and soaring over land (positive values) from flightless and burst-adapted flyers (negative values) (Fig. 10A). Visualisation of the shape changes along dimension 1 indicates that birds capable of pursuit hunting and soaring over land have a more sinuous lateral semicircular canal (Fig. 10B–C). However, examination of the plot of scores along the x and y axes of dimension 1 of the phylogenetic 2B-PLS indicate that the relationship documented by this axis results from extreme values in two pairs of sister taxa: *Larus argentatus* and *Creagrus furcatus*, and *Phalacrocorax harrisi* and *Phalacrocorax carbo* (Fig. 10D; Fig. 11A).

When the influential taxa labelled in Figure 10D are excluded from the analysis, phylogenetic 2B-PLS analysis of labyrinth morphology (PC1–65) against flight style (PCo1–Pco7) does not return a significant multivariate association between labyrinth shape and flight capability (Fig. S3D–F). This indicates that the apparent multivariate association shown in Fig. 10 results only from the comparative morphologies of two sister-taxon pairs, and does not characterise ‘background’ patterns of avian labyrinth morphology and flying style, at least so far as they are captured by our dataset.

Discussion

Comparative results. We find evidence for two sets of relationships between phenotypic traits (including flight behaviour) and the morphology of the endosseous labyrinth in birds.

(1) The size of the vestibular system (centroid size) is best explained by body mass in flying birds. Brachial index, a proxy for wing kinematics, explains an additional, small portion of the variance in labyrinth size, especially when flightless birds are included (Table 3; flightless birds have high brachial indices). These relationships contain a moderate-to-strong amount of phylogenetic signal (λ values from 0.66 to 0.80 for the best model across all 100 trees), and indicate that larger birds and flying birds have longer semicircular canals than their evolutionary relatives. We find an allometric coefficient of 0.2 for labyrinth centroid size (Table 3). This indicates that larger birds have proportionally (though not absolutely) smaller labyrinths, and is consistent with a predicted slope of $^{1}/_{12}$ - $^{1}/_{3}$ based on dynamic or geometric similarity of skull size in relation to body mass (Jones & Spells 1963). Our result is consistent with previous evidence for negative allometry of labyrinth size with body mass in mammals (Spoor et al. 2007; Lebrun et al. 2010; Alloing-Séguier et al. 2013), and with the presence of proportionally larger labyrinths in more agile primates and other mammals (Spoor et al. 2007).

(2) The first principal component axis (PC1) correlates strongly, and negatively, to body mass (Table 6). It therefore captures allometric changes in the shapes of the semicircular canals. Larger birds have negative values of PC1, corresponding to more anteriorly located anterior vertical canals, more ventrally located posterior vertical canals, proportionally smaller lateral canals, and a larger angle between the planes of the anterior and lateral canals (Figs 4A, 5). This relationship is characterised by strong phylogenetic signal (λ ~ 1.0; Table 6), indicating that the shape changes occur with respect to close evolutionary relatives (i.e. they are modifications of a phylogenetically determined 'baseline' morphology). Allometric shape change in strepsirhine primates and diprotodontan

marsupials is similar to that of birds in that the lateral canal is proportionally smaller in larger-bodied taxa. However, it differs in that the posterior canal is located further dorsally in larger strepsirrhines and diprotodontans, but further ventrally in larger birds (Fig. 4; Lebrun et al., 2010; Aloing-Seguier et al., 2013).

We also find equivocal evidence for links between flying style and labyrinth shape. Firstly, we find that allometric changes in labyrinth morphology (PC1; Fig. 4) correlate with the first principal coordinates axis (PCo1; Fig. 9), which differentiates birds using flight modes such as sally hunting, intermittent bounding and use of cluttered airspace from those that use pelagic soaring and submerged aquatic feeding. However, this correlation is found only by ordinary two-block partial least squares analysis (Fig. S1), and not when using phylogenetic two-block partial least squares (Fig. S3). Furthermore, such a correspondence could be explained by the size-dependency of both PC1 and PCo1, rather than a direct causative relationship between these flight modes and labyrinth shape. Secondly, using phylogenetic two-block partial least squares (2B-PLS), we found a relationship between a set of principal component axes that jointly describe changes in the sinuosity of the lateral canal (Fig. 10B) with a principal coordinates axis (PCo2) that differentiates birds that use flight modes such as pursuit hunting and soaring over land from those that are flightless or use burst adapted flight. This correlation was determined by the occurrence of two pairs of taxa with extreme values of the 2B-PLS dimensions (Fig. 10D), and apparently does not characterise background patterns of evolution (Fig. S3). Nevertheless, these taxon pairs represent relatively shallow evolutionary divergences that gave rise to large variation in locomotory style or habitual visual field: *Creagrus furcatus*, the swallowtailed gull is the only nocturnal seabird (compared to a diurnal gull, *Larus argentatus*), and *Phalacrocorax harrisi* is flightless, compared to a flying great cormorant (*Phalacrocorax carbo*). Our taxon sample was not designed to test possibility that substantial evolutionary changes in visual field and flight mode influence the sinuosity of the lateral canals (indicated in Fig. 10B), but this warrants further investigation.

Ubiquitous phylogenetic signal in form/function relationships for the labyrinth. The relationships highlighted above contain at least moderate phylogenetic signal, as does the negative correlation of canal orthogonality with vestibular sensitivity documented in mammals by Berlin et al. (2013; $\lambda = 0.682$). This indicates that the morphology of the vestibular system varies across the phylogeny, but is modified in consistent ways by changes in body mass. Therefore, birds with similar phenotypic traits may not have similar semicircular canals unless they are also close evolutionary relatives. 'Phylogenetic signal' in the relationship between traits indicates that the residual, unexplained, variance in the relationship evolves in a Brownian-like fashion on the tree. This may occur when other, unconsidered, traits influence the dependent variable (e.g. labyrinth size), and are themselves phylogenetic-correlated. For example, in the context of an integrated vestibulo-ocular system competing for space with other organs in the braincase, those traits might relate to the visual field (Kemp & Kirk, 2014), or to the relative sizes of the brain, cochlea or external ears (Martin, 2009; Davies et al. 2013).

Phylogenetic signal has also been demonstrated for the labyrinth morphologies of strepsirrhine primates (Lebrun et al., 2010), diprotodontan marsupials (Alloing-Seguier et al., 2013), and musteloid carnivorans (Gröhe et al., 2015). Qualitative inferences of form-function relationships were also made for these groups. However, our analysis and those of Malinzak et al. (2012) and Berlin et al. (2013) are the only studies to quantitatively analyse both phylogenetic and functional (or ecological) signals in the morphology of the labyrinth together in a single analytical framework (i.e. phylogenetic generalised least squares regression allowing λ to vary). This approach has important advantages compared to analysing separately for phylogenetic signal and trait correlations, because both ecology (function) and morphology (form) both evolve along the branches of the same phylogeny. This can cause the spurious inference of correlation when non-phylogenetic methods are used to test form-function relationships (e.g. Felsenstein, 1985).

Phylogenetic independent contrasts (used to analyse labyrinth morphology by Georgi et al., 2013) provide only a partial solution to this problem because they assume, but do not demonstrate, strong phylogenetic signal (i.e. $\lambda = 1.0$) in the relationship between traits. This is problematic because the strength of phylogenetic signal in the relationship between traits cannot be estimated a priori by analysis of individual traits. Therefore, it is not possible to determine in advance when phylogenetic independent contrasts should be used. Notably, even traits involved in strict form-function relationships (these relationships lack phylogenetic signal [$\lambda = 0$]; Motani & Schmitz, 2011) can be individually characterised by strong phylogenetic signal (also discussed by Lebrun et al., 2010). In this situation, the traits underwent evolutionary change on the tree, but the relationship between them did not. The solution to this problem is to jointly analyse phylogenetic signal and form-function correlation together, as done here and by Malinzak et al. (2012), Berlin et al. (2013) and Motani & Schmitz (2012).

As an illustration of the pitfalls of interpreting phylogenetic comparative results, note that Gröhe et al. (2015) reported evidence for differentiation of labyrinth morphologies among musteloid carnivorans with different ecologies (e.g. aquatic, terrestrial, fossorial) when using non-phylogenetic statistical tests. However, they found no correlation when using phylogenetic comparative methods (phylogenetic ANOVA). Their interpretation was that both phylogeny and function influenced the morphology of the musteloid labyrinth (Gröhe et al., 2015). However, this would only be correct only if there was evidence for both non-zero values of λ, and also of a statistically significant correlation between the traits. The correct interpretation of the results of Gröhe et al. (2015) is that changes in ecology along phylogenetic lineages are not correlated to changes in labyrinth morphology along the same lineages. This suggests that they found no statistical evidence for form-function relationships in musteloid labyrinth morphology.

We find a similar result regarding the association of allometric change in labyrinth morphology (PC1; Fig. 6) with the set of flight variables described by PCo1 (Fig. 9). A significant association between PC1 and PCo1 is found when using ordinary 2B-PLS, but not when using phylogenetic 2B-PLS (Fig. S3). This suggests that PC1 and PCo1 are associated among the taxa that we studied, but that this association does not result from co-evolution of PC1 and PCo1 along phylogenetic lineages. Instead, it can be explained by non-independence of observations made on closely related pairs of taxa (phylogenetic autocorrelation; Felsenstein, 1985).

The lack of statistical support for an association between PC1 and PCo1 here, and between musteloid labyrinth morphology and ecology in Gröhe et al. (2015) may be due to low statistical power rather than the absence of a relationship. Loss of statistical power can occur when using phylogeny-based statistical methods. The effective sample size of these methods is determined by the number of independent evolutionary origins of the dependent trait variable, which is smaller than the total number of species analysed. In the current example passerines, a speciose clade, have both small body size (influencing their PC1 scores because PC1 represents allometric shape change), and intermittent bounding flight (represented by PCo1; Fig. 9). However, both traits were inherited from a single common ancestor, and do not provide strong evidence of a form-function relationship. To address this, future studies will need to include a larger sample of taxa, specifically targeting larger numbers of independent evolutionary transitions between the focal ecologies (e.g. flight/flightlessness, subaqueous diving, nocturnality, pursuit hunting, soaring).

Endosseous labyrinth as a palaeoecological proxy. Based on our findings, ecological information for fossil birds might most readily be inferred from the centroid size of the vestibular portion of the endosseous labyrinth relative to estimated body mass. This relationship provides information on flight ability, because flightless birds have proportionally smaller systems of semicircular canals than their flying relatives (Fig. 3; Fig. 11A). This may allow the use of vestibular morphology to make inferences about the origins of powered flight on the avian stem lineage using fossils. For example, the early avialan *Archaeopteryx* has a vestibular organ with similar proportional features to those seen in modern birds (Domínguez et al., 2004). These features (posterior canal extends ventral to lateral canal; anterior canal elongated and reflexed; Domínguez et al., 2004) plausibly relate to the accommodation of longer canals within the same physical volume, and suggest that *Archaeopteryx* has proportionally longer semicircular canals than those seen in other non-avian dinosaurs where those features are absent (e.g. Witmer et al., 2008; Azuma et al., 2016). Nevertheless, some flying birds have similar vestibular sizes (relative to body mass) to those of flightless birds (Fig. 3; the tufted duck *Aythya fuligula*, and flamingo *Phoenicopterus ruber*). Further investigation of independent evolutionary transitions to flightlessness is required to determine how the lengths and shapes of the semicircular canals change along single lineages making the evolutionary transition to flightlessness, and whether there is a distinction between recent evolutionary origins of flightlessness (e.g. the Falkland steamer duck *Tachyeres brachypterus* and the flightless cormorant *Phalacrocorax harrisi*), and ancient ones (e.g. flightless ratites). Until then, the vestibular system nevertheless indicates the occurrence of powered flight, when the vestibular sizes of extinct taxa fall well within the range of modern flying birds.

Functional interpretations of comparative results. The effect of labyrinth size (or canal lengths) on the functional properties of the vestibular system is well understood. These effects are consistent with our findings from regression analysis that that manoeuvrability (brachial index) explains a portion of the variance in labyrinth size explains a portion of the variance in labyrinth size independently of body mass, and our observation that most flying birds have proportionally longer semicircular canals than flightless taxa (Fig. 3). Longer canals have a larger radius of curvature than shorter canals, and therefore inertially displace more endolymphatic fluid per unit rotation (differences in cross-sectional diameter may also affect these basic mechanical properties [Hullar, 2006], but this has not yet been studied in detail). This results in a greater deflection of the cupula and so greater mechanoelectrical transduction during head rotation, yielding greater biomechanical and afferent nervous vestibular sensitivity (Yang & Hullar, 2007). High sensitivity to small displacements may be important in flight, allowing for subtle early reflex corrections to head rotations that maintain balance and gaze stability. This has also been hypothesised for agile arboreal locomotion in primates, which correlates to increased radius of curvature in comparative studies (Spoor et al., 2007).

Recently, Kemp & Kirk (2014) showed that eye size and visual acuity have stronger relationships with labyrinth size than does agility in mammals. In fact, they showed that the best explanatory model for labyrinth size (radius of curvature) in mammals included body mass, eye size and visual acuity, but not agility. This suggests that agile mammals generally have greater larger eyes and visual acuity, and that this requires more responsive gaze stabilisation. In other words, the relationship between canal lengths and agility is indirect: the larger labyrinth of more agile mammals is required specifically in order to service their higher visual acuities by enhancing gaze stabilisation.

Birds have the proportionally largest eyes among tetrapods (Brooke et al., 1999; Howland et al., 2004). We suggest that the function of the labyrinth in maintaining visual fixation, and therefore enabling high visual acuity, may therefore explain why birds also have proportionally large labyrinths (Jones & Spells, 1963). We hypothesise the existence of a lower limit to labyrinth size, below which visual acuity is compromised by inadequate optokinetic response processing. If this is true, then the size of the labyrinth may correlate to eye size and visual acuity in all vertebrate species that depend substantially on vision. Because of their large eyes, birds have been cited as support for the hypothesis that there is a positive relationship between locomotory speed and eye size ('Leuckart's Law'; Brooke et al., 1999). However, Hall & Heesy (2010) found that the fastest flying birds (Anseriformes) actually have relatively small eyes, particularly compared with predatory birds such as Falconiformes. We show here that Anseriformes also have proportionally smaller labyrinths (*Aythya fuligula* and *Tachyeres brachypterus* [flightless]) than Falconiformes (e.g. *Falco tinnunculus*) and other raptorial birds (e.g. *Aquila chrysaetos*) (Fig. 3A). Although we do not have data on eye size for the birds included in our study, these observations are consistent with the hypothesis of a relationship between eye size/visual acuity and labyrinth size in birds that is similar to that of mammals (Kemp & Kirk, 2014). Tytoine owls provide a further test of this relationship because they have large eyes (e.g. Brooke et al., 1999) but low visual acuity as their optical anatomy maximises sensitivity to low light levels by sacrificing fine spatial resolution (e.g. Martin 1986; Orlowski et al., 2012). Consistent with their lowered visual acuity, tytoines also have proportionally small labyrinths (Fig. 11). If visual acuity is indeed a more important determinant of labyrinth size in tetrapods than is agility (or the ability to fly), this may also explain the apparent paradox of proportionally small labyrinth sizes in bats, which have low visual acuity, and have similar relative labyrinth sizes to those to other mammals (Davies et al., 2013).

Unlike the situation regarding labyrinth size, the effect of labyrinth shape (i.e. proportional or topographic changes) on vestibular sensitivity is poorly constrained. For example, it has often been suggested that the relative sizes of individual canals are linked to the planes in which most rotation takes place during locomotion, or that differences in canal outline shape may affect sensitivity (Hullar, 2006; Cox & Jeffery, 2010; Ekdale, 2016), and a theoretical framework for understanding the physical effects of changes to the vestibular organ on canal sensitivity is well established (Cox & Jeffery, 2010). Nevertheless, few comparative studies have found strong statistical evidence that the specific shapes observed among species correspond to their locomotory behaviours (but see Yi & Norell [2015] for an example in squamates). Contrary to prior expectations, Malinzak et al. (2012) found in primates that axes of maximum sensitivity (based on relative lengths of the canals) do not align with axes of rapid or slow head rotations (calculated from kinematic experiments). Instead, primates with faster head rotations have more orthogonal canal orientations, which provide more homogeneous sensitivity among different rotational planes. Because flight requires high agility, this observation predicts that flying birds (and especially agile flying birds) should have more orthogonal semicircular canal configurations than non-flying birds.

However, we find little evidence for a link between specific labyrinth morphologies and flying styles in birds. Critically, the angles between the planes of the semicircular canals of birds show no correlation to wing kinematics (brachial index), and are typically greater than 90° (Fig. 4: 94.0° [anterior-lateral canals], 98.0° [anterior-posterior canals], 93.0° [anterior-posterior canals]). Given the fact that they can fly, it is reasonable to suggest that birds are more agile than most mammals, so it is surprising that the inter-canal angles of birds deviate more strongly from 90° than the mean inter-canal angles seen in mammals (Berlin et al., 2013: 84.5°, 91.9°, and 90.3° respectively). These observations seem to violate the prediction that more agile taxa should have more orthogonal canal configurations (Malinzak et al. 2012).

Although we did not find evidence for effects of wing kinematics and flying style on the morphology of the avian semicircular canals, we did find strong evidence of allometric shape changes, including changes in the angle between the planes of the anterior and lateral semicircular canals: small birds generally have a smaller angle between the planes of the anterior and lateral canals (Fig. 4A). Small birds also have an anterior canal that is rotated posteriorly (Figs 3A, 5). Both changes represent prominent modifications of the anterior semicircular canal, and inspection of our virtual models suggests that these result from spatial constraints imposed by the brain, mostly by the mesencephalon and cerebellum. Both the brain (Jerison, 1973) and labyrinth (Jones & Spells, 1963) scale with negative allometry in birds (and other tetrapods). Therefore, constraint on the availability of space is most intense in small-bodied species. This is illustrated by the smallest bird in our dataset, the hummingbird *Selasphorus rufus*, which shows extremely strong posterior rotation of the anterior canal (Fig. 3A; Fig. 12C–D), and in the woodcock *Scolopax ruficola* (Fig. 7D; Fig. 12A–B), which seems to accommodate a proportionally long anterior canal by tilting it laterally, resulting in a proportionally low angle between the anterior and lateral canals (Fig. 4A). The barn owl *Tyto alba* also has a relatively smaller labyrinth than the burrowing owl *Athene cunicularia* (Fig. 11), which may result from the presence of an highly enlarged cochlea in tytoine owls (Fig. 12; Walsh and Milner, 2011: fig. 11.5D). Similarly, Davies et al. (2013) found evidence for spatial constraint on the size of the semicircular canals, imposed by the cochlea (which co-occupies the petrosal bone together with the semicircular canals in mammals) in echolocating bats. Both tytoine owls and echolocating bats also have low visual acuity compared to most other birds in our study (discussed above). This may also be linked to their small labyrinth sizes, and therefore provide evidence of spatially-imposed trade-off between the sensory capabilities of the vestibular and auditory organs.

Based on these observations, we suggest that spatial occupation imposes a strong constraint on the geometry of the semicircular canal system in birds. Spatial constraint resulting from large labyrinth and large brain size in birds may limit the extent of tuning of the shape of the avian labyrinth in response to specific functional demands compared to other tetrapods such as mammals and squamates. In particular, this may explain why the inter-canal plane angles of birds deviate more strongly from orthogonality than those of mammals, and therefore have lower theoretical sensitivity than could be achieved by a more orthogonal configuration (Malinzak et al., 2012; Berlin et al., 2013).

Nevertheless, other aspects of allometric shape change in the bird labyrinth are shared with those of mammals. Our regression analyses show that smaller birds have proportionately longer lateral semicircular canals, and this is also seen in primates and marsupials (Lebrun et al., 2010; Aloing-Segurier et al., 2013; other groups have not yet been studied). This proportional difference may relate to the greater potential for manoeuvrability in smaller-bodied birds and mammals. In support of this hypothesis, Cox & Jeffery (2010) documented a correlation of the proportional size of the lateral canal with agility in mammals. Nevertheless, brachial index, which correlates with wing kinematics and manoeuvrability in flying birds (Nudds et al., 2007), does not correlate strongly with any major axis of shape change recovered by our analyses, calling this hypothesis into question in birds, unless other aspects of wing shape (e.g., hand- to arm-wing ratio: Videler, 2005) or body size confound the manoeuvrability signal of the humerus-ulna ratio.

Cox & Jeffery (2010) also suggested that relative length of the lateral canal may correlate to the occurrence of 3D locomotory styles (e.g. flying, swimming versus terrestrial locomotion). Our present taxon sample includes few evolutionary transitions between flying, flightless and swimming modes of locomotion and has little power to test this hypothesis in birds. Furthermore, Smith & Clarke (2012) observed few qualitative differences among the labyrinths of swimming versus non-swimming charadriiform birds. Quantitative work targeting a sample of taxa that documents evolutionary transitions between these locomotory modes is required to test their effect on labyrinth morphology.

Possible causes of the apparent absence of links between flying style and labyrinth shape in birds. In addition to our regression analyses, we also used two-block partial least squares (2B-PLS) to analyse the association between labyrinth morphology and flying style. Overall, we document considerable variation in avian vestibular morphology (Fig. 6), and 2B-PLS is a powerful technique for testing associations between blocks of multivariate data. Nevertheless, we find only equivocal evidence of such associations (discussed above). This suggests that flying style is not among the most important determinants of avian labyrinth shape. Nevertheless, other causes could explain also the apparent absence of this relationship. For example, it is possible that our method for characterising flying style is not capturing the relevant patterns of locomotion that are actually linked to labyrinth morphology. It is difficult to remedy this problem. Although anatomical measurement provide appealing proxies for flight kinematics, previous authors have noted the complex interdependency of brachial index (Wang & Clarke, 2014) and of external wing shape (Taylor 2014; Wang & Clarke 2015) on both function and phylogeny, and that such proxies may capture some, but not all aspects of avian flying styles (Taylor 2014; Wang & Clarke 2014, 2015). However, approaches such as that used by Malinzak et al. (2012), which calculated axes of rapid or slow head rotations from kinematic experiments, provide a potential future line of enquiry.

It is also possible that there is actually not a strict one-to-one relationship between flight kinematics and labyrinth shape in birds. It is possible, for example, that multiple labyrinth morphologies can produce the same neurosensory performance, in an example of many-to-one mapping (Rabbitt et al., 2004; David et al., 2010). Alternatively, evolutionary changes in visual acuity, changes in the visual environment through which a bird flies, changes in how that environment is perceived, and changes in the how optical sensory afferents are processed by the brain (e.g. Gaede et al., 2016) might be equally as important as labyrinth morphology for maintaining adequate head stabilisation reflexes. For example, Wylie and Frost (1996) demonstrated that the spatial planes of the optokinetic system of birds are organised with respect to the eye muscles rather than the semicircular canals. Therefore, the coevolution of the physical structure and orientation of the eyes, with that of the semicircular canals may provide an example of multi-system many-to-one mapping. This hypothesis could be tested by characterising eye parameters for individual bird species and jointly analysing their evolution together with that of labyrinth morphology.

Recent experimental manipulations of the visual fields of flying birds (Bhagavtula et al., 2014; budgerigars), and especially hummingbirds (Goller & Altschuler, 2014; Dakin et al., 2016) has demonstrated the use of global optic field flow in stabilising flight (Goller & Altschuler, 2014) and avoiding collisions (Bhagavtula et al., 2014; Dakin et al., 2016). Optical afferents are processed in the pretectal nucleus lentiformis mesencephali (LM) as part of the accessory optic system pathway that projects to folia IV-VIII, IXcd and X of the cerebellum (Pakan and Wylie, 2006). This pathway is primarily important for global optic scene analysis, although input to folium IXcd also forms part of the optokinetic response for gaze stabilisation (Pakan and Wylie, 2006; Iwaniuk et al., 2007). Hummingbirds exhibit unparalleled stabilised sustained hovering and the ability to fly in reverse. Perhaps surprisingly therefore, their semicircular canals are not exceptionally large in relation to body mass when compared to other birds, and are not exceptionally different in shape to those of other birds (Fig. 3A). Nevertheless, they possess a hypertrophied LM region (Iwaniuk and Wylie, 2007). This recently has been shown to be potentially unique in vertebrates in that it has rapid sensitivity to relative changes in global scene features in all directions (Gaede et al., 2017; this region in other tetrapods is more sensitive to front-to-back motion of the global visual field). This highlights the potential importance of global visual motion for control of balance in flight, and indicates that evolutionary adaptation of the optokinetic response may be critical importance in the evolution of tetrapod locomotion. It is likely therefore that only some evolutionary changes in locomotory style might be reflected directly by changes in the physical structure of the labyrinth.

The physical structure of the semicircular canals may be somewhat tuned to particular locomotory abilities of individual species. Nevertheless, studies of labyrinth morphology in both mammals and birds have demonstrated that the morphologies of the semicircular canals frequently deviate from those that might theoretically be expected to optimise vestibular sensitivity to rotations in key planes of head motion (Hullar, 2006; Malinzak et al. 2012). For example, the plane of each canal often deviates strongly from the anatomical planes of the head. This has been shown in crocodiles, dinosaurs, birds (Witmer et al., 2008; Milner & Walsh, 2009), squamates (Olori, 2010) and mammals (Cox & Jeffery, 2008). In such cases, stimulation of multiple canals will occur when the head is rotated around the anatomical axes (Rabbit, 1999). Furthermore, a strong degree of variability in canal intersection angle (up to 30 degrees deviation from othogonality) and extraocular muscle alignment has been demonstrated in mammals (Cox & Jeffery, 2008; Berlin et al., 2013), and we find on average even stronger deviations from orthogonality in birds. Both Malinzak et al. (2012) and Berlin et al. (2013) found that deviation from orthogonality is detrimental to vestibular sensitivity, but is nevertheless apparently widespread (see also Billet et al. 2012, in sloths).

We have shown that much of the variation in labyrinth shape that is seen among birds (41.8% of shape variation is explained by PC1) may be linked to physical constraints regarding the space available to the vestibular organ (Figs 11–12). In addition to the apparent allometric constraints demonstrated here, constraints could also be imposed by braincase size and structure, variation in orbit position within the skull, and variation in eye size among other factors (Cox & Jeffery, 2008). This raises questions about how the vestibular system maintains its function when spatial constraints act to modify its form.

One possibility is that neural processing of vestibular and optic flow field stimuli can ameliorate the effects of sub-optimal vestibular sensitivity incurred by deviations of the semi-circular canals from orthogonal anatomical planes. Wylie & Frost (1999) showed that although such processing does occur in an optimal frame of reference in pigeons, peak sensitivity in the vertical planes (i.e., monitored by the anterior and posterior semicircular canals) actually occurs at an angle of 45 degrees to the midline. Consequently, ostensibly poor labyrinth configurations may not have an appreciable effect on balance or gaze stabilisation, but instead represent neurosensory 'compromises' to accommodate competing ecological adaptations, such as larger eye or cochlea size in nocturnal taxa and skull-size reduction in small-bodied taxa. A 'fully-optimised' neurosensory system (in the theoretical sense) may also be less effective in real-world situations, in which species must be capable of performing and rapidly switching between a wide variety of locomotory behaviours. If so, more generalised visual and vestibular signals may offer a more resilient information source that is more easily tuned through plasticity of central nervous system control.

The possibility that sub-optimal labyrinth morphologies can function in a sensitive yet resilient manner highlights the observation that the vestibular system functions as an integral part of a complex proprioceptive system of balance that includes visual, vestibular and integumental signals, and not as an isolated accelerometer. The interplay between neural and sensory components of the systems controlling balance and gaze stabilisation are clearly complex. This makes the precise determination of the significance of small morphological changes for ecological inferences challenging, and perhaps impossible.

Birds have increased the lengths of the semicircular canals compared to other tetrapods (Jones & Spells, 1963). Our comparative analysis of the avian labyrinth indicates that this has come at the expense of other aspects of morphological 'tuning', such as orthogonality among canal planes, contrasting with enhancement of orthogonality in agile mammals. Spatial constraints, phylogeny, and allometric effects play more significant roles in determining the geometry of the avian labyrinth than do wing kinematics, flying style, or even the ability to fly at all. Nevertheless, our study demonstrates the potential of the labyrinth for future analysis, especially when combined with other lines of evidence from skull size, shape, eye parameters and neuroanatomy.

Acknowledgements

CT scanning and data processing were supported by NERC grant NE/H012176/1 to SAW and NE/E008380/1 to Paul Barrett, and by funding from the European Union's Horizon 2020 research and innovation programme 2014–2018 under grant agreement 677774 (ERC Starting Grant: TEMPO). We thank Samantha Giles and Matthew Friedman for access to computational facilities and support. We thank Joanne Cooper, Judith White (Natural History Museum bird collection, Tring, United Kingdom) and Bob McGowan (National Museums Scotland) for access to specimens. We also thank Armin Schmitt for assistance with reformatting of image stacks for online archiving.

Author contributions

ES-J conducted the research, including segmenting the labyrinths, other data collection and preliminary statistical analyses. He also drafted portions of the manuscript. RAC assisted with data processing and methodological choices, rendered digital images and movies, and provided critical comments on the manuscript. SAW designed the taxon sample, scanned the specimens, and drafted portions of the manuscript. RBJB oversaw all aspects of the research, designed and conducted the analyses and wrote the manuscript with the other authors.

References

Adams DC, Felice RN (2014) Assessing trait covariation and morphological integration on phylogenies using evolutionary covariance matrices. *PLoS ONE*, **9**, e94335.

Adams DC, Otarola-Castillo E (2013) geomorph: an R package for the collection and analysis of geometric morphometric shape data. *Meth Ecol Evol* **4**, 393–399.

Alloing-Séguier L, Sánchez-Villagra M, Lee MSY, et al. (2013) The bony labyrinth in diprotodontian marsupial mammals: diversity in extant and extinct forms and relationships with size and phylogeny. *J MammEvol* **20**, 191–198.

Azuma Y, Xu X, Shibata M, et al. (2016) A bizarre theropod from the Early Cretaceous of Japan highlighting mosaic evolution among coelurosaurians. *Sci Rep* **6**, 1–13.

Berlin JC, Kirk EC, Rowe TB (2013) Functional implications of ubiquitous semicircular canal non-orthogonality in mammals. *PLoS ONE* **8**, e79585.

Bhagavatula PS, Claudianos C, Ibbotson MR, Srinivasan MV (2011) Optic flow cues guide flight in birds. *Curr Biol* **21**, 1794–1799.

Billet G, Hautier L, Asher R, et al. (2012) High morphological variation of vestibular system accompanies slow and infrequent locomotion in three-toed sloths. *Proc R Soc B* **279**, 3932–3939.

Bilo D, Bilo A (1978) Wind stimuli control and vestibular and optokinetic reflexes in the pigeon. *Naturwissenschaften* **65**,161–162.

Bookstein FL (1997) Landmark methods for forms without landmarks: morphometrics of group differences in outline shape. *Medical Image Anal* **1**,97–118.

Brooke M de L, Hanley S, Laughlin SB (1999) The scaling of eye size with body mass in birds. *Proc R Soc Lond B* 266, 405–412.

Bruderer B, Peter D, Boldt A, et al. (2010) Wing-beat characteristics of birds recorded with tracking radar and cine camera. *Ibis* **152**, 272–291.

Burnham KP, Anderson D (2001) *Model Selection and Multi-Model Inference: a Practical Information-Theoretic Approach*. New York: Springer. 488p.

Close RA, Rayfield EJ (2012) Functional morphometric analysis of the furcula in Mesozoic birds. *PLoS ONE* **7**, e36664.

Cox PG, Jeffery N (2008) Geometry of the semicircular canals and extraocular muscles in rodents, lagomorphs, felids and modern humans. *J Anat* **213**, 83–596.

Cox PG, Jeffery N (2010) Semicircular canals and agility: the influence of size and shape measures. *J Anat* **216**, 37–47.

Dakin R, Fellows TK, Altshuler DL (2016) Visual guidance of forward flight in hummingbirds reveals control based on image features instead of pattern velocity. *PNAS* **113**, 8849–8854.

David R,Droulez J, Allain R, et al. (2010) Motion from the past. A new method to infer vestibular capacities of extinct species. *Compt RendPalevol* **9**, 397–410.

David R, Stoessel A, Berthoz A, Spoor F, Bennequin D (2016) Assessing morphology and function of the semicircular duct system: introducing new *in-situ* visualization and software toolbox. *Sci Rep*, doi.org/10.1038/srep32772.

Davies KTJ, Bates PJJ, Maryanto I, et al. (2013) The evolution of bat vestibular systems in the face of potential antagonistic selection pressures for flight and echolocation. *PLoS ONE* **8**, e61998.

del Hoyo J, Elliott A, **Sargatal J** (1992) *Handbook of the birds of the world. Volume 1: Ostrich to Ducks*. Lynx Edicions. 696p.

del Hoyo J, Elliott A, **Sargatal J** (1994) *Handbook of the birds of the world. Volume 2: New World Vulture to Guineafowl*. Lynx Edicions. 638p.

del Hoyo J, Elliott A, **Sargatal J** (1996) *Handbook of the birds of the world. Volume 3: Hoatzin to Auks*. Lynx Edicions. 824p.

del Hoyo J, Elliott A, **Sargatal J** (1997) *Handbook of the birds of the world. Volume 4: Sandgrouse to Cuckoos*. Lynx Edicions. 679p.

del Hoyo J, Elliott A, **Sargatal J** (1999) *Handbook of the birds of the world. Volume 5: Barn-Owls to Hummingbirds*. Lynx Edicions. 759p.

del Hoyo J, Elliott A, **Sargatal J** (2001) *Handbook of the birds of the world, M. Volume 6: Mousebirds to Hornbills*. Lynx Edicions. 589p.

del Hoyo J, Elliott A, **Sargatal J** (2002) *Handbook of the birds of the world. Volume 7: Jacamars to Woodpeckers*. Lynx Edicions. 613p.

del Hoyo J, Elliott A, **Christie DA** (2005) *Handbook of the birds of the world. Volume 10: Cuckoo Shrikes to Thrushes*. Lynx Edicions. 895p.

del Hoyo J, Elliott A, **Christie DA** (2006) *Handbook of the birds of the world. Volume 11: Old World Flycatchers to Old World Warblers*. Lynx Edicions. 798p.

del Hoyo J, Elliott A, **Christie DA** (2008) *Handbook of the birds of the world. Volume 13: Penduline-tits to Shrikes*. Lynx Edicions. 879p.

del Hoyo J, Elliott A, **Christie DA** (2009) *Handbook of the birds of the world. Volume 14: Bush-shrikes to Old World Sparrows*. Lynx Edicions. 893p.

del Hoyo J, Elliott A, **Christie DA** (2010) *Handbook of the birds of the world. Volume 15: Weavers to New World Warblers*. Lynx Edicions. 879p.

Dial KP (2003) Evolution of avian locomotion: correlates of flight Style, locomotor modules, nesting biology, body size, development, and the origin of flapping flight. *Auk* **120**, 941–952.

Domínguez P, Milner AC, Ketcham RA, et al. (2004) The avian nature of the brain and inner ear of *Archaeopteryx*. *Nature* **430**, 666–669.

Ekdale EG (2016) Form and function of the mammalian inner ear. *J Anat* **228**, 324–337.

Ericson PGP, Anderson CL, Britton T, Elzanowski A, Johansson US, Källersjö M, Ohlson JI, Parsons TJ, Zuccon D, Mayr G (2006) Diversification of Neoaves: integration of molecular sequence data and fossils. *Biol Lett* **2**, 543–547.

Felsenstein J (1985) Phylogenies and the comparative method. *Am Naturalist* **125**, 1–15.

Foth C, Tischlinger H, Rauhut OWM (2014) New specimen of Archaeopteryx provides insights into the evolution of pennaceous feathers. *Nature* **511**, 79–82.

Gaede AH, Goller B, Lam JPM, Wylie DR, Altshuler DL (2016) Neurons responsive to global visual motion have unique tuning properties in hummingbirds. *Curr Biol* **26**, 279–285.

Gauthier JA, Padian K (1985) Phylogenetic, functional, and aerodynamic analyses of the origin of birds and their flight. In: *The Beginnings of Birds: Proceedings of the International Archaeopteryx Conference, Eichstätt, 1984*. (eds Hecht MK, Ostrom JH, Viohl G, Wellnhofer P), pp. 185-197. Eichstätt:Freunde des Jura-Museums Eichstätt.

Georgi JA, Sipla JS, Forster CA (2013). Turning semicircular canal function on its head: dinosaurs and a novel vestibular analysis. *PLoS ONE* **8**, e58517.

Goller B, Altshuler DL (2014) Hummingbirds control hovering flight by stabilizing visual motion. *Proc Natl Acad Sci USA* 111, 18375–18380.

Gower JC (1975) Generalized Procrustes analysis. *Psychometrika* **40**,33–50.

Grafen A (1989) The phylogenetic regression. *Phil Trans R Soc B* **326**, 119–157.

Grohé C, ZJ Tseng, Lebrun R, et al. (2015) Bony labyrinth shape variation in extant Carnivora: a case study of Musteloidea. *J Anat* **228**, 366–83.

Gunz P Mitteroecker P (2013) Semilandmarks: a method for quantifying curves and surfaces. *Hystrix* **24**, 103–109.

Gunz P, Mitteroecker P, Bookstein FL (2005) Semilandmarks in three dimensions. In: *Modern Morphometrics in Physical Anthropology*. (ed. Slice DE). New York: Kluwer Aca- demic/Plenum Publishers, pp. 73–98.

Gunz P, Ramsier M, Kuhrig M, et al. (2012) The mammalian bony labyrinth reconsidered, introducing a comprehensive geometric morphometric approach. *J Anat* **220**, 529–543.

Hackett SJ, Kimball RT, Reddy S, Bowie RCK, Braun EL, Brain MJ, Chojnowski JL, Cox WA, Han K-L, Harshman J, Huddleston CJ, Marks BD, Miglia KJ, Moore WS, Sheldon FH, Steadman DW, Witt CC, Yuri T (2008) A phylogenomic study of birds reveals their evolutionary history. *Science* **320**, 1763–1768.

Hadžiselimović H, Savković L (1964) Appearance of semicircular canals in birds in relation to mode of life. *Acta Anatomica* **57**, 306–315.

Hall MI, Heesy CP (2010) Eye size, flight speed and Leuckart’s Law in birds. *J Zool* **283,** 291–297.

Howland HC, Merola S, Basarab JR (2004) The allometry and scaling of the size of vertebrate eyes. *Vision Res* **44**, 2043–2065.

Hullar TE (2006) Semicircular canal geometry, afferent sensitivity, and animal behavior. *Anat Rec A Discov Mol Cell Evol Biol* **288**, 466–472.

Iwaniuk AN, Wylie DRW (2008) Neural specialization for hovering in hummingbirds: hypertrophy of the pretectal nucleus lentiformis mesencephalic. *J Comp Neurol* **500**, 211–221.

Jerison HJ (1973) *Evolution of the brain and intelligence*. London: Academic Press.

Jetz W, Thomas GH, Joy JB, et al. (2012). The global diversity of birds in space and time. *Nature* **491**, 444–448.

Jones GM, Spells KE (1963) A theoretical and comparative study of the functional dependence of the semicircular canal upon its physical dimensions. *Proc R Soc Lond B* **157**, 403–419.

Kemp AD, Kirk EC (2014) Eye size and visual acuity influence vestibular anatomy in mammals. *Anat Rec* 297, 781–790.

Kendall DG (1977) The diffusion of shape. *Adv App Prob* **9**, 428–430.

Lebrun R, de León MP, Tafforeau P, et al. (2010) Deep evolutionary roots of strepsirrhine primate labyrinthine morphology. *J Anat* **216**, 368–380.

Leigh J, Brandt T (1993) A re-evaluation of the vestibule-ocular reflex: new ideas of its purpose, properties, neural substrate and disorders. *Neurology* 43, 1288–1295.

Longrich NR, Vinther J, Meng Q, et al. (2012) Primitive wing feather arrangement in *Archaeopteryx lithographica* and *Anchiornis huxleyi*. *Curr Biol* **22**, 1–6.

Malinzak MD, Kaya RF, HullarTE (2012) Locomotor head movements and semicircular canal morphology in primates. *PNAS* **109**, 17914–17919.

Martin GR (1986) Sensory capacities and the nocturnal habits of owls (Strigiformes). *Ibis* **128**, 266–277.

Martin GR (2009) What is binocular vision for? A birds' eye view. *J Vision* **9**, 1–19.

Milner AC, Walsh SA (2009). Avian brain evolution: new data from Palaeogene birds (Lower Eocene) from England. *Zool Linn Soc* **155**, 198–219.

Motani R, Schmitz L (2011) Phylogenetic versus functional signals in the evolution of form-function relationships in terrestrial vision. *Evolution*, 65, 2245–2257.

Muller M (1994) Semicircular duct dimensions and sensitivity of the vertebrate vestibular system. *J Theor Biol* **167**, 239–256.

Nagelkerke NJD (1991) A note on a general definition of the coefficient of determination. *Biometrika* **78**, 691–692.

Norberg UM (1990) *Vertebrate flight: mechanics, physiology, morphology, ecology and evolution*. Berlin: Springer-Verlag. 291 p.

Nudds RL, Dyke GJ, Rayner JMV (2007) Avian brachial index and wing kinematics: putting movement back into bones. *J Zool* **272**, 218–226.

Olori JC (2010). Digital endocasts of the cranial cavity and osseous labyrinth of the burrowing snake *Uropeltis woodmasoni* (Alethinophidia: Uropeltidae). *Copeia*, **1**, 14–26.

Orlowski J, Harmening W, Wagner H (2012) Night vision in barn owls: visual acuity and contrast sensitivity under dark adaptation. *J Vision* **12**, 4.

Padian K, Chiappe LM (1998) The origin and evolution of birds. *Biol Rev* **73**, 1–42.

Pagel M *(*1999*)* Inferring the historical patterns of biological evolution*. Nature,* **401***,* 877–884*.*

Paradis E, Claude J, Strimmer K (2004). APE: analyses of phylogenetics and evolution in R language. *Bioinformatics* **20**, 289–290.

Pennycuick CJ (2008) *Modelling the flying bird*. London: Academic Press. 480p.

Pfaff C, Martin T, Ruf I. (2015) Bony labyrinth morphometry indicates locomotor adaptations in the squirrel-related clade (Rodentia, Mammalia). *Proc R Soc B* **282**, 20150744.

Pinheiro J, Bates D, DebRoy S, et al. (2015) nlme: Linear and Nonlinear Mixed Effects Models. R package version 3.1-122, <URL: http://CRAN.R-project.org/package=nlme>.

Rabbitt RD (1999) Directional coding of three-dimensional movements by the vestibular semicircular canals. *Biol Cybern* **80**,417–431.

Rabbitt RD, Damiano ER, Grant JW (2004) Biomechanics of the semicircular canals and otolith organs. In: *The vestibular system* (eds Highstein S, Fay RR, Popper AN). New York: Springer, pp 153–201.

Rayner JMV (1988) Form and function in vertebrate flight. In: *Current Ornithology* Vol. 5 (ed. Johnston RF) New York and London: Plenum Press, pp. 1–66.

Rohlf FJ, Slice D (1990). Extensions of the Procrustes method for the optimal superimposition of landmarks. *Syst Zool* **39**, 40–59.

Rohlf FJ, Corti M (2000) Use of two-block partial least-squares to study covariation in shape. *Syst Biol* **49**, 740–753.

Schlager S (2016) Morpho: Calculations and Visualisations Related to Geometric Morphometrics. R package version 2.3.1.1. https://CRAN.R-project.org/package=Morpho

Sievwright H, MacLeod N (2012) Eigensurface analysis, ecology, and modelling of morphological adaptation in the falconiform humerus (Falconiformes: Aves). *Zool Linn Soc* **165**, 390–419.

Silcox MT, Bloch JI, Boyer DM, et al. (2009) Semicircular canal system in early primates. *J Hum Evol* **56**, 315–327.

Simons ELR (2010) Forelimb skeletal morphology and flight mode evolution in pelecaniform birds. *Zoology* **113**, 39–46.

Sipla J, Spoor F (2008) The physics and physiology of palance. In: *Sensory Evolution on the Threshold, Adaptations in Secondarily Aquatic Vertebrates* (eds Thewissen JGM, Nummela S), Berkeley: University of California Press, pp. 227-232.

Smith NA, Clarke JA (2012) Endocranial anatomy of the charadriiformes: sensory system variation and the evolution of wing-propelled diving. *PloS ONE* **7**, e49584.

Spoor F (2003) The semicircular canal system and locomotor behaviour, with special reference to hominin evolution. *Cour Forsch Senckenberg* **243**, 93–104.

Spoor F, Zonneveld F (1998) Comparative review of the human bony labyrinth. *Year Phys Anthrop* **41**, 211–251.

Spoor F, Bajpai S, Hussain ST, et al. (2002) Vestibular evidence for the evolution of aquatic behaviour in early cetaceans. *Nature* **417**, 163–166.

Spoor, F. Garland T, Krovitz G, et al. (2007) The primate semicircular canal system and locomotion. *PNAS* **104**, 10808–10812.

Sugiura N (1978) Further analysis of the data by Akaike's Information Criterion and the Finite Corrections. *Commun Stat Theory Meth A* **7**, 13–26.

Taylor G (2014) Adaptation in avian wing design. In: *Evolutionary Biomechanics* (eds Taylor G, Thomas A). Oxford: Oxford University Press. 152p.

ten Kate JH (1969) The oculo-vestibulo reflex of the growing pike. Unpublished Ph.D. Thesis, University of Groningen, The Netherlands.

Thewissen JGM, Nummela S (2008) Sensory evolution in aquatic tetrapods: toward and integrative approach. In *Sensory Biology on the Threshold: Adaptations in secondarily aquatic vertebrates* (eds Thewissen JGM, Nummela S). Berkeley: University of California Press, pp. 333-340.

Videler JJ (2005) *Avian Flight*. Oxford: Oxford University Press.

Viscor G, Fuster JF (1987) Relationship between morphological parameters in birds with different flying habits. *Comp Biochem Physiol A Comp Physiol* **87**, 231–249.

Walsh SA, Milner AC (2011) Evolution of the avian brain and senses. In: *Living dinosaurs: the evolutionary history of modern birds* (eds Dyke G, Kaiser G). John Wiley & Sons, pp. 282–305.

Walsh SA, Barrett PM, Milner AC, et al. (2009) Inner ear anatomy is a proxy for deducing auditory capability and behaviour in reptiles and birds. *Proc Royal Soc B* **276**, 1355–1360.

Walsh SA, Iwaniuk AN, Knoll MA, et al. (2013) Avian cerebellar floccular fossa size is not a proxy for flying ability in birds. *PLoS ONE* **8**, e67176.

Walsh SA, Zhe-XI L, Barrett P (2014) Modern imaging techniques as a window to prehistoric auditory worlds. *In Insights from Comparative Hearing Research* (eds Köppl C, Manley G) Springer Verlag, pp. 227–261.

Wang X, Clarke JA (2014) Phylogeny and forelimb disparity in waterbirds. *Evolution* **68**, 2847–2860.

Wang X, Clarke JA (2015) The evolution of avian wing shape and previously unrecognised trends in covert feathers. *Proc Roy Soc B* **282**, 20151935.

Wang X, McGowan AJ, Dyke GJ (2011) Avian wing proportions and flight styles: first step towards predicting the flight modes of Mesozoic birds. *PLoS ONE* **6**, e28672.

Warrick DR, Bundle MWK, Dial P (2002) Bird maneuvering flight: blurred bodies, clear heads. *Int Comp Biol* **42**, 141–148.

Webster M, Sheets H (2010) A Practical Introduction to Landmark-based geometric Morphometrics. In: *Quantitative Methods in Paleobiology*. (eds Alroy J, Hunt G). Paleontological Society Papers **16**, pp. 163–188.

Wilson VJ, Melville-Jones G (1979) *Mammalian Vestibular Physiology*. New York: Springer. 365p.

Witmer LM, Chatterjee S, Franzosa J, et al. (2003) Neuroanatomy of flying reptiles and implications for flight, posture and behaviour. *Nature* **425**, 950–953.

Witmer LM, Ridgely RC, Dufeau DL, et al. (2008) Using CT to peer into the past: 3D visualisation of the brain and ear regions of birds, crocodiles and nonavian dinosaurs. In: *Anatomical Imaging: Towards a New Morphology* (eds Endo H, Frey R), pp. 67–87. Tokyo: Springer Verlag. 105 p.

Wylie DR, Frost BJ (1999) Complex spike activity of Purkinje cells in the ventral uvula and nodulus of pigeons in response to translational optic flow. Journal of Neurophysiology, 81: 256–266.

Xu X, Zhou Z, Wang X, et al. (2003) Four-winged dinosaurs from China. *Nature* **421**, 335–340.

Xu X, Zhou Z, Dudley R, et al. (2014) An integrative approach to understanding bird origins. *Science* 346(6215): 1253293.

Xu X, Zheng X, Sullivan C, Wang X, et al. (2015) A bizarre Jurassic maniraptoran theropod with preserved evidence of membranous wings. *Nature* **521**, 70–73.

Yang AZ, Hullar TE (2007) Relationship of semicircular canal size to vestibular-nerve afferent sensitivity in mammals. *J Neurophysiol* **98**, 3197–3205.

Yi H, Norell MA (2015) The burrowing origin of modern snakes. *Sci Adv* **1**, 1–5.

Zelditch ML, Swiderski DL, Sheets HD, et al. (2012) *Geometric morphometrics for biologists: a primer*. Amsterdam: Academic Press. 488p.

Supplementary Information

Appendix S1. Discussion of flight categories

Fig. S1. Summary of 2B-PLS results comparing multivariate flight style to PC shape axes for endosseous labyrinth morphology including outliers and including all shape axes.

Fig. S2. Summary of 2B-PLS results comparing multivariate flight style to PC shape axes for endosseous labyrinth morphology including outliers and including all shape axes except PC1.

Fig. S3. Summary of 2B-PLS results comparing multivariate flight style to PC shape axes for endosseous labyrinth morphology including outliers and including all shape axes, excluding four outlier taxa.

Table S1. Results of regressions of labyrinth inter-canal angles on body mass and brachial index.

Table S2. Results of regressions of positivised deviations of labyrinth inter-canal angles from 90° on body mass and brachial index.

Table S3. Results of regressions of summed positivised deviations of labyrinth inter-canal angles from 90° on body mass and brachial index.

Table S4. Regression model comparison results for principal component PC4.

Table S5. Regression model comparison results for principal component PC5.

Table S6. Regression model comparison results for principal component PC6.

Table S7. Regression model comparison results for principal component PC7.

Table S8. Regression model comparison results for principal component PC8.

Figure captions

Fig. 1. Rendering of the skull of *Podargus strigoides* indicating the position of the endosseous semicircular canals. An opaque rendering is shown in (A), and a transparent rendering through which the endosseous canals (minus the vestibule and cochlear canal) are visible is shown in (B). Identity is indicated with colour for the anterior [=rostral] canal (blue), posterior [=caudal] canal (green), and lateral [=horizontal] canal (yellow). Scale bar: 10 mm.

Fig. 2. Process of segmenting (A), skeletonising (B), and landmarking (C) the avian labyrinth. The four separate 3D voxel models are shown in grey (entire endosseous labyrinth), blue (anterior [=rostral] semicircular canal), green (posterior [=caudal] semicircular canal), and yellow (lateral [=horizontal] semicircular canal). Abbreviations: AA, ampulla of the anterior semicircular canal; ASC, anterior semicircular canal; C, cochlear duct; CC, crus communis; LA, ampulla of the lateral canal; LSC, lateral semicircular canal; PA, ampulla of the posterior semicircular canal; PSC, posterior semicircular canal; VE, vestibule. In panel (C), conventional landmarks at the ends of each semicircular canal are indicated by large yellow spheres and numbered 1–6. Sliding semilandmarks defining the course of each semicircular canal are indicated by small yellow spheres.

Fig. 3. Plots of (A) labyrinth centroid size on body mass, with point sizes scaled to brachial index (strong, multivariate relationship; Table 3), (B) labyrinth centroid size on brachial index (no relationship; Table 3), and (C) residuals of the relationship between labyrinth

centroid size and body mass (Table 3, upper panel, model 2, variables $\log_{10}$-transformed) on brachial index. Points are coloured according to mutually exclusive subset categories in our multivariate flight categorisation for visualisation purposes only, and are white when none of these categories is present in a species. The decision as to which flight categories should be represented here was informed by the inferred significance of pursuit hunting for labyrinth morphology (see *Results*). Labyrinth models are shown in lateral view for selected taxa to illustrate the extremes of the relationship of labyrinth size with body mass.

Figure 4. Plots of inter-canal angles versus body mass for the angles between (A) the anterior semicircular canal (ASC) and lateral semicircular canal (LSC), (B) the anterior and posterior semicircular canals (PSC), and (C) the lateral and posterior semicircular canals. Points are coloured according to a mutually exclusive subset categories in our multivariate flight categorisation for visualisation purposes only, and are white when none of these categories is present in a species. Labyrinth models are shown in anterior (A), dorsal (B) and lateral (C) views for selected taxa to illustrate the extremes of inter-canal angles among the sampled taxa.

Fig. 5. Landmark configurations corresponding to the mean shape (grey symbols) and deformations along principal component axis PC1–PC3 (black symbols). Deformations correspond to the highest negative (‘min’) and positive (‘max’) score on each PC axis. Deformations are shown in three views corresponding approximately to the orthogonal

planes of each of the three semicircular canals. Videos showing these deformations, and deformations of other PC axes (PC1–PC12) are available in the Supplementary Information.

Fig. 6. 3D digital models of the endosseous labyrinths of selected species in lateral view, showing morphological changes among species distributed along PC1 (top row), PC2 (middle row) and PC3 (bottom row).

Fig. 7. Plots of principal component scores (A) PC1 versus PC2, and (B) PC1 versus PC3. The proportions of total shape variance explained by each axis are indicated in brackets (and see Table 4). Points are coloured according to three mutually exclusive categories in our multivariate flight categorisation, and greyed when none of these categories is present in a species. Numbers indicate taxa as denoted in Table 1. Labyrinth models of selected taxa are shown in lateral view to illustrate extreme values of PC1 and PC2.

Fig. 8. Regressions of principal component axes 1–3 (PC1–PC3) on body mass (A,C,E) with point sizes scaled to brachial index, and on brachial index (B,D,F). PC1 shows a strongly significant relationship with body mass (A) (Table 6), but other axes shown here show no relationship with either body mass or brachial index (Tables 6–8). Points are coloured according to three mutually exclusive categories in our multivariate flight categorisation, and greyed when none of these categories is present in a species.

Fig. 9. Interpretation of principal coordinates axis 1 (PCo1) for flying style. The distribution of taxa scored as possessing each flying style (black discs) is shown along the first principal coordinates axis (PCo1; horizontal axis). Flight categories that show clustering towards either end of PCo1 are indicated in black, others are in grey.

Fig. 10. Dimension 1 of our non-allometric two-block partial least squares (2B-PLS) analysis describes a multivariate association between a composite flying style variable (PCo2) and shape change in the labyrinth described by the principal components axes PC6, PC7, and PC11. (A) The distribution of taxa scored as possessing each flying style (black discs) is shown along the second principal coordinates axis (PCo2; horizontal axis). Flight categories that show clustering towards either end of PCo2 are indicated in black, others are in grey. (B–C) Labyrinth shape deformations (black symbols) implied by change of PC scores along dimension 1 seen in lateral (A) and anterior (B) views, as compared to the mean shape (grey symbols). Key shape differences are increasing sinuosity of the lateral canal and an increase in the angle between the planes of the anterior and posterior canals at negative shape scores on Dimension 1. (D) Ordination of taxa based on x and y scores of dimension 1 showing that two influential sister-taxon pairs act as influential datapoints in the analysis. The labyrinth models of these taxa are shown on the plot in lateral view.

Fig. 11. Relationship between labyrinth centroid size and body mass (taken from Fig. 3A), with owls and outlier taxon pairs from 2B-PLS indicated. *Tyto alba*, the barn owl, has a proportionally reduced labyrinth and enlarged cochlea compared to *Athene cunicularia*, the

burrowing owl. 3D virtual models of the labyrinths of *A. cunicularia* (B)–(C) and *Tyto alba* (D)–(E) are shown in lateral (B), (D), and anterior (C), (E) to illustrate this.

Fig. 12. Spatial constraints on the morphology of the avian semicircular canals, illustrated by 3D scan reconstruction models of (A)–(B), *Scolopax rusticola* the woodcock, (C)–(D), *Selasphorus rufus*, the rufous hummingbird, and (E)–(F), *Stuthio camelus*, the ostrich. (A), (C), and (E) show the endocast (purple) in context of the cranium (grey) in left lateral view. (B), (D), and (F) show closer images in anterolateral view with magnification of the semicircular canals. *Scolopax rusticola* and *Selasphorus rufus* show strong evidence of spatial deformation of the semicircular canals due to occupation of space by the brain, *Struthio camelus* does not. For example, the angle between the planes of the anterior and lateral canal is low in *Scolopax rusticola* and *Selasphorus rufus* (indicated) but close to orthogonal in *Struthio camelus* (indicated).

Tables

No.	**Taxon**	**Order: family**	**Common name**
1	*Apteryx haastii*	Struthioniformes: Apterygidae	Great Spotted Kiwi
2	*Casuarius casuarius*	Struthioniformes: Casuariidae	Southern Cassowary
3	*Struthio camelus*	Struthioniformes: Struthionidae	Ostrich
4	*Rhynchotus rufescens*	Tinamiformes: Tinamidae	Red-winged Tinamou
5	*Aythya fuligula*	Anseriformes: Anatidae	Tufted Duck
6	*Tachyeres brachypterus*	Anseriformes: Anatidae	Falkland Steamerduck
7	*Coturnix coturnix*	Galliformes: Phasianidae	Common Quail
8	*Gallus gallus*	Galliformes: Phasianidae	Red Junglefowl
9	*Phasianus colchicus*	Galliformes: Phasianidae	Common Pheasant
10	*Caprimulgus europaeus*	Caprimulgiformes: Caprimulgidae	European Nightjar
11	*Podargus strigoides*	Caprimulgiformes: Podargidae	Tawny Frogmouth
12	*Steatornis caripensis*	Caprimulgiformes: Steatornithidae	Oilbird
13	*Apus apus*	Apodiformes: Apodidae	Common Swift
14	*Selasphorus rufus*	Apodiformes: Trochilidae	Rufous Hummingbird
15	*Columba livia*	Columbiformes: Columbidae	Rock Dove
16	*Cuculus canorus*	Cuculiformes: Cuculidae	Common Cuckoo
17	*Grus grus*	Gruiformes: Gruidae	Common Crane
18	*Alca torda*	Charadriiformes: Alcidae	Razorbill
19	*Gavia immer*	Gaviiformes: Gaviidae	Great Northern Diver
20	*Haematopus ostralegus*	Charadriiformes: Haematopodidae	Eurasian Oystercatcher
21	*Creagrus furcatus*	Charadriiformes: Laridae	Swallow-tailed Gull
22	*Larus argentatus*	Charadriiformes: Laridae	European Herring Gull
23	*Actitis hypoleucos*	Charadriiformes: Scolopacidae	Common Sandpiper
24	*Scolopax rusticola*	Charadriiformes: Scolopacidae	Eurasian woodcock
25	*Gelochelidon nilotica*	Charadriiformes: Sternidae	Gull-billed Tern
26	*Ardea cinerea*	Ciconiiformes: Ardeidae	Grey Heron

27	*Balaeniceps rex*	Ciconiiformes: Balaenicipitidae	Shoebill
28	*Ciconia ciconia*	Ciconiiformes: Ciconiidae	White Stork
29	*Ciconia nigra*	Ciconiiformes: Ciconiidae	Black Stork
30	*Diomedea exulans*	Procellariiformes: Diomedeidae	Wandering Albatross
31	*Pelagodroma marina*	Procellariiformes: Hydrobatidae	White-Faced Storm Petrel
32	*Fulmarus glacialis*	Procellariiformes: Procellariidae	Northern Fulmar
33	*Fregata magnificens*	Pelecaniformes: Fregatidae	Magnificent Frigatebird
34	*Phaethon lepturus*	Pelecaniformes: Phaethontidae	White-Tailed Tropicbird
35	*Phalacrocorax carbo*	Pelecaniformes: Phalacrocoracidae	Great Cormorant
36	*Phalacrocorax harrisi*	Pelecaniformes: Phalacrocoracidae	Flightless Cormorant
37	*Phoenicopterus ruber*	Phoenicopteriformes: Phoenicopteridae	American Flamingo
38	*Podiceps cristatus*	Podicepediformes: Podicepedidae	Great Crested Grebe
39	*Opisthocomus hoazin*	Opisthocomiformes: Opisthocomidae	Hoatzin
40	*Aquila chrysaetos*	Falconiformes: Accipitridae	Golden Eagle
41	*Buteo buteo*	Falconiformes: Accipitridae	Common Buzzard
42	*Vultur gryphus*	Falconiformes: Cathartidae	Andean Condor
43	*Pandion haliaetus*	Falconiformes: Pandionidae	Osprey
44	*Sagittarius serpentarius*	Falconiformes: Sagittariidae	Secretarybird
45	*Athene cunicularia*	Strigiformes: Strigidae	Burrowing Owl
46	*Tyto alba*	Strigiformes: Tytonidae	Barn Owl
47	*Alcedo atthis*	Coraciiformes: Alcedinidae	Common Kingfisher
48	*Coracias garrulus*	Coraciiformes: Coraciidae	European Roller
49	*Dendrocopos major*	Piciformes: Picidae	Great Spotted Woodpecker
50	*Ramphastos dicolorus*	Piciformes: Rhamphastidae	Green-billed Toucan
51	*Trogon curucui*	Trogoniformes: Trogonidae	Blue-crowned Trogon
52	*Circus cyaneus*	Falconiformes: Accipitridae	Hen Harrier
53	*Cathartes* sp.	Falconiformes: Cathartidae	New world vulture
54	*Falco subbuteo*	Falconiformes: Falconidae	Eurasian Hobby
55	*Falco tinnunculus*	Falconiformes: Falconidae	Common Kestrel

56	*Ara macao*	Psittaciformes: Psittacidae	Scarlet Macaw
57	*Melopsittacus undulatus*	Psittaciformes: Psittacidae	Budgerigar
58	*Psittacus erithacus*	Psittaciformes: Psittacidae	African Grey Parrot
59	*Corvus corax*	Passeriformes: Corvidae	Common Raven
60	*Dicrurus paradiseus*	Passeriformes: Dicruridae	Greater Racket-tailed Drongo
61	*Taeniopygia guttata*	Passeriformes: Estrildidae	Timor Zebra Finch
62	*Acanthorhynchus superciliosus*	Passeriformes: Meliphagidae	Western Spinebill
63	*Passer domesticus*	Passeriformes: Passeridae	House Sparrow
64	*Luscinia megarhynchos*	Passeriformes: Turdidae	Common Nightingale

Table 1. List of taxa included in the dataset for the present study. Further data, including specimen numbers, is given in Walsh et al. (2009, 2013). “No.” is the number used to indicate each taxon in figures.

Flight categories	**Pennycuick (2008)**	**Bruderer et al. (2010)**	**Close and Rayfield (2012)**
Soaring	yes	no	yes
Dynamic soaring	no	yes	no
Static soaring	no	yes	no
Continuous flapping	yes	yes	yes
Flap-gliding	yes	yes	yes
Flapping and gliding	no	yes	no
Intermittent bounding	yes	no	yes
Partial bounding	no	yes	no
Flap-bounding	no	yes	no
Burst-adapted	no	no	yes
Subaqueous flight	no	no	yes

Table 2. Flight classifications proposed by previous studies based on Pennycuick (2008). Yes/no are used to indicate which categories were included in each analysis.

	Model	**λ**	**Variable**	**Coefficient**	**p-value**	**AICc**	**AICc-weight**	**R^2**
	Including flightless birds							
1**	size ~ brachial index (BI) + body mass (mass)	0.71	intercept	0.65	<0.001	-145.4	0.98	0.82
			log10(BI)	-0.39	<0.001			
			log10(mass)	0.2	<0.001			
2	size ~ mass	0.81	intercept	0.66	<0.001	-137.1	0.02	0.79

			log10(mass)	0.19	<0.001			
3	size ~ BI	0.33	intercept	1.24	<0.001	-40.6	<0.01	0.00
			log10(BI)	0.29	0.202			
	Excluding flightless birds							
1**	size ~ mass	0.79	intercept	0.68	<0.001	-130.2	0.73	0.796
			log10(mass)	-0.5	<0.001			
2*	size ~ BI + mass	0.70	intercept	0.82	<0.001	-128.8	0.27	0.799
			log10(BI)	-0.16	0.038			
			log10(mass)	0.20	<0.001			
3	size ~ BI	0.81	intercept	1.24	<0.001	-36.6	0.00	-0.028
			log10(BI)	-0.04	0.834			

Table 3. Results of phylogenetic generalised least squares (pGLS) regressions of labyrinth centroid size ('size') on body mass and brachial index, with flightless species included (above), and excluded (below). All models were fitted allowing variation in phylogenetic signal (λ; Pagel 1999) to be estimated as part of the model fitting process. Models are rank-ordered by AICc weight so the best model (**) is at the top. All variables are $\log_{10}$-transformed. N = 62 for analyses of all birds, and N = 57 for analyses excluding flightless birds. Results for just one phylogeny are shown, but results for the other 99 are similar and are summarised in the text. R^2 is the generalised coefficient of determination described by Nagelkerke (1991), and negative values indicate that a model is worse than an intercept-only null model. Results for just one phylogenetic topology are presented here. But analyses on alternative topologies recovered essentially identical results.

	Model	**λ**	**Variable**	**Coefficient**	**p-value**	**AICc**	**AICc-weight**	**R^2**

1**	Brachial index (BI) ~ log10(Csize) + log10(mass)	0.81	(Intercept)	0.3	0.004	-129.8	0.97	0.115
			log10(Csize)	-0.5	<0.001			
			log10(mass)	0.13	<0.001			
3	BI ~ log10(mass)	0.86	(Intercept)	-0.03	0.614	-121.5	0.02	-0.05
			log10(mass)	0.03	0.047			
6	BI ~ log10(Csize)	0.91	(Intercept)	0.04	0.696	-120.9	0.01	-0.059
			log10(Csize)	0.02	0.784			

Table 4. Results of phylogenetic generalised least squares (pGLS) regressions of brachial index (BI) on body mass and centroid size (below). All models were fitted allowing variation in phylogenetic signal (λ; Pagel 1999) to be estimated as part of the model fitting process. Models are rank-ordered by AICc weight so the best model (**) is at the top. All variables are log$_{10}$-transformed. N = 62 for all analyses in this table. Results for just one phylogeny are shown, but results for the other 99 are similar and are summarised in the text. R^2 is the generalised coefficient of determination described by Nagelkerke (1991), and negative values indicate that a model is worse than an intercept-only null model. Results for just one phylogenetic topology are presented here. But analyses on alternative topologies recovered essentially identical results.

	PC1	PC2	PC3	PC4	PC5	PC6	PC7	PC8	PC9	PC10	PC11	PC12
Proportion of Variance	0.418	0.157	0.083	0.048	0.044	0.04	0.034	0.03	0.021	0.019	0.016	0.014
Proportion of Variance (excluding PC1)	NA	0.269	0.143	0.082	0.076	0.068	0.058	0.051	0.037	0.033	0.027	0.023
Cumulative Proportion	0.418	0.575	0.658	0.706	0.75	0.79	0.824	0.853	0.875	0.894	0.909	0.923

Table 5. Proportions of variance explained by principal component (PC) axes for bird labyrinths. The proportion of variance excluding PC1 describes the proportion of non-allometric shape variance explained by each of the other PC axes shown in this table (PC2–PC12). The selection of PC axes to display here is guided by our finding that relatively minor shape axes (PC11) may describe ecologically significant variation in form (and also see Cooney et al., 2017 for beak morphology).

	Model	λ	Variable	Coefficient	p-value	AICc	AICc-weight	R^2
1**	PC 1 ~ body mass (mass)	1.05	intercept	0.2	<0.001	-143.3	0.86	0.306
			log10(mass)	-0.08	<0.001			
2*	PC 1 ~ brachial index (BI) + mass	1.1	intercept	0.13	0.006	-139.6	0.14	0.290
			log10(BI)	-0.15	<0.001			
			log10(mass)	-0.06	<0.001			
3	PC 1 ~ BI	1.05	intercept	-0.02	0.639	-115.5	<0.01	-0.085
			log10(BI)	-0.13	0.322			

Table 6. Results of phylogenetic generalised least squares (pGLS) regressions of labyrinth first principal component (PC1) axis on body mass and brachial index, allowing variation in phylogenetic signal (λ; Pagel, 1999) to be estimated as part of the model fitting process. Models are rank-ordered by AICc weight so the best model (**) is at the top. Models with similar AICc weights to the best model are indicated with **; and other models with non-negligible AICc weights (up to one-tenth with weight of the best model) are indicated with *. All variables are $\log_{10}$-transformed. N = 62 for all analyses in this table. Results for just one phylogeny are shown, but results for the other 99 are similar and are summarised in the text. R^2 is the generalised coefficient of determination described by Nagelkerke (1991), and negative values indicate that a model is worse than an intercept-only null model.

	Model	**λ**	**Variable**	**Coefficient**	**p-value**	**AICc**	**AICc weight**	**R^2**
1**	PC 2 ~ BI	0.93	(Intercept)	0.03	0.384	-156.2	0.91	-0.036
			log10(BI)	0.08	0.428			
2	PC 2 ~ mass	0.93	(Intercept)	0.01	0.78	-151.4	0.08	-0.119
			log10(mass)	0.01	0.571			
3	PC 2 ~ BI + mass	0.93	(Intercept)	0.01	0.759	-146.9	<0.01	-0.161
			log10(BI)	0.07	0.498			
			log10(mass)	0	0.694			

Table 7. Results of phylogenetic generalised least squares (pGLS) regression of labyrinth second principal component (PC2) axis on body mass and brachial index, allowing variation in phylogenetic signal (λ; Pagel, 1999) to be estimated as part of the model fitting process. Models are rank-ordered by AICc weight so the best model (**) is at the top. Models with similar AICc weights to the best model are indicated with **; and other models with non-negligible AICc weights (up to one-tenth with weight of the best model) are indicated with *. All variables are log$_{10}$-transformed. N = 62 for all analyses in this table. Results for just one phylogeny are shown, but results for the other 99 are similar and are summarised in the text. R^2 is the generalised coefficient of determination described by Nagelkerke (1991), and negative values indicate that a model is worse than an intercept-only null model.

	Model	λ	Variable	Coefficient	p-value	AICc	AICc-weight	R^2
1**	PC 3 ~ brachial index (BI)	0.84	intercept	0	0.894	-186.4	0.90	-0.049
			log10(BI)	0.05	0.549			
2*	PC 3 ~ body mass (mass)	0.86	intercept	-0.01	0.789	-181.9	0.09	-0.128
			log10(mass)	0	0.568			
3	PC 3 ~ BI + mass	0.85	intercept	-0.01	0.816	-176.6	<0.01	-0.185
			log10(BI)	0.04	0.65			
			log10(mass)	0	0.668			

Table 8. Results of phylogenetic generalised least squares (pGLS) -regressions of labyrinth third principal component (PC3) axis on body mass and brachial index, allowing variation in phylogenetic signal (λ; Pagel, 1999) to be estimated as part of the model fitting process. Models are rank-ordered by AICc weight so the best model (**) is at the top. Models with non-negligible AICc weights (up to one-tenth with weight of the best model) are indicated with *. All variables are $\log_{10}$-transformed. N = 62 for all analyses in this table. Results for just one phylogeny are shown, but results for the other 99 are similar and are summarised in the text. R^2 is the generalised coefficient of determination described by Nagelkerke (1991), and negative values indicate that a model is worse than an intercept-only null model.

Dimension	**1**	**2**	**3**	**4**	**5**	**6**	**7**
PC1	**-0.969***	-0.092	0.104	0.033	-0.069	0.064	-0.028
PC2	-0.049	0.797	0.039	0.379	0.07	0.019	0.007
PC3	0.167	0.01	0.573	-0.146	0.213	0.212	0
PC4	0.123	-0.054	0.057	0.356	-0.54	0.328	-0.142
PC5	0.068	-0.507	0.147	0.42	0.131	0.045	0.294
PC6	0.068	-0.05	0.276	-0.03	-0.622	-0.222	-0.109
PC7	-0.004	-0.109	0.155	0.061	0.001	-0.523	0.032
PC8	-0.016	-0.028	0.43	0.056	0.259	-0.189	-0.477
PC9	-0.032	0.022	0.387	0.006	-0.035	0.323	0.255
PC10	-0.015	0.117	0.095	-0.046	0.027	-0.314	0.589
PC11	0.008	-0.19	-0.293	0.332	0.192	0.008	-0.011
…	…	…	…	…	…	…	…
PCo1	**-0.946***	0.299	-0.108	-0.048	0.015	0.007	0.028
PCo2	-0.273	-0.867	-0.183	0.366	0.038	-0.054	-0.047
PCo3	0.152	0.129	-0.953	-0.037	0.052	0.215	-0.044
PCo4	0.066	0.31	0.014	0.853	0.01	0.058	0.411
PCo5	0.019	0.047	-0.182	0.018	-0.724	-0.661	0.041
PCo6	0.034	0.202	-0.027	0.293	0.401	-0.453	-0.711
PCo7	-0.029	0.051	0.114	0.223	-0.557	0.552	-0.565
PLS_cor	0.692	0.514	0.546	0.377	0.541	0.428	0.455
PLS_cov	0.014	0.004	0.002	0.001	0.001	0.001	0.001
PLS_pcov	0.869	0.087	0.023	0.008	0.007	0.003	0.003

Table 9. Ordinary 2B-PLS results including influential taxa. Input variables with high loadings on dimension 1, which contributes 87% of the variance explained by the association, are indicated in bold type and by *. PC1–PC65 were analysed, but only PC1–PC11 are shown here as subsequent PC axes (PC12–PC65) have negligible loadings on all dimensions.

X	**PC1**	**PC2**	**PC3**	**PC4**	**PC5**	**PC6**	**PC7**	**PC8**	**PC9**	**PC10**	**PC11**	**…**
Dimension 1	**0.47***	0.08	0.07	0.14	0.09	**0.28***	**0.43***	0.04	0.14	0.10	**0.39***	…
Dimension 2	**0.76***	0.06	0.11	0.17	0.20	0.18	**0.28***	0.12	0.08	0.09	**0.35***	…
Y	**PCo1**	**PCo2**	**PCo3**	**PCo4**	**PCo5**	**PCo6**	**PCo7**					
Dimension 1	**0.47***	**0.84***	0.14	0.06	0.17	0.03	0.11					
Dimension 2	**0.81***	**0.47***	0.30	0.05	0.11	0.03	0.15					

Table 10. Summary of phylogenetic 2B-PLS results including influential taxa. This table presents the median absolute loading for each input variable across the full set of phylogenetic 2B-PLS analyses for exploratory purposes, demonstrating that PC1, PC6, PC7, and PC11 are important parts of the apparent association between flying style and labyrinth shape.

Dimension	**1**	**2**	**3**	**4**	**5**	**6**	**7**
PC2	0.03	-0.033	-0.203	0.77	0.054	0.195	-0.545
PC3	0.197	0.107	-0.499	0.188	0.002	0.398	0.483
PC4	-0.018	0.51	0.174	0.331	-0.404	-0.241	0.182
PC5	0.112	0.632	-0.098	-0.38	-0.142	0.415	-0.289
PC6	**-0.408***	0.282	-0.122	0.003	0.018	-0.496	-0.226
PC7	**-0.601***	0.267	-0.302	0.015	0.223	0.12	0.145
PC8	-0.007	-0.213	-0.647	-0.074	-0.314	-0.358	0.137
PC9	0.177	-0.118	-0.298	-0.274	-0.367	-0.02	-0.475
PC10	0.175	0.106	-0.236	-0.15	0.714	-0.185	-0.159
PC11	**0.598***	0.326	-0.04	0.122	0.143	-0.388	0.107
….	**…**	…	…	…	…	…	…
PCo1	0.006	-0.933	0.135	-0.176	0.152	-0.17	-0.171
PCo2	**0.961***	0.066	-0.081	-0.037	0.03	-0.235	-0.091
PCo3	0.119	0.052	0.829	0.442	0.213	0.212	-0.103
PCo4	-0.031	0.012	-0.408	0.32	0.288	0.291	-0.75
PCo5	-0.21	0.219	0.006	0.072	0.61	-0.728	-0.008
PCo6	0.056	-0.273	-0.326	0.767	-0.014	-0.043	0.475
PCo7	-0.121	0.018	0.124	0.277	-0.689	-0.504	-0.404
pPLS_cor	0.641	0.393	0.415	0.314	0.433	0.186	0.14
pPLS_cov	0	0	0	0	0	0	0
pPLS_pcov	0.426	0.183	0.165	0.088	0.064	0.04	0.035
pPLS_cov2	0	0	0	0	0	0	0
pPLS_pcov2	0.708	0.062	0.111	0.066	0.026	0.02	0.009

Table 11. Phylogenetic 2B-PLS results for tree 1, excluding PC1 (i.e. non-allometric analysis). Other phylogenies yield similar results that are summarised in Fig. 9. Input variables with high loadings on dimension 1, which contributes 87% of the variance explained by the association, are indicated in bold type and by *.This association is

visualised in Fig. 10. PC1–PC65 were analysed, but only PC1–PC11 are shown here as subsequent PC axes (PC12–PC65) have negligible loadings on all dimensions.

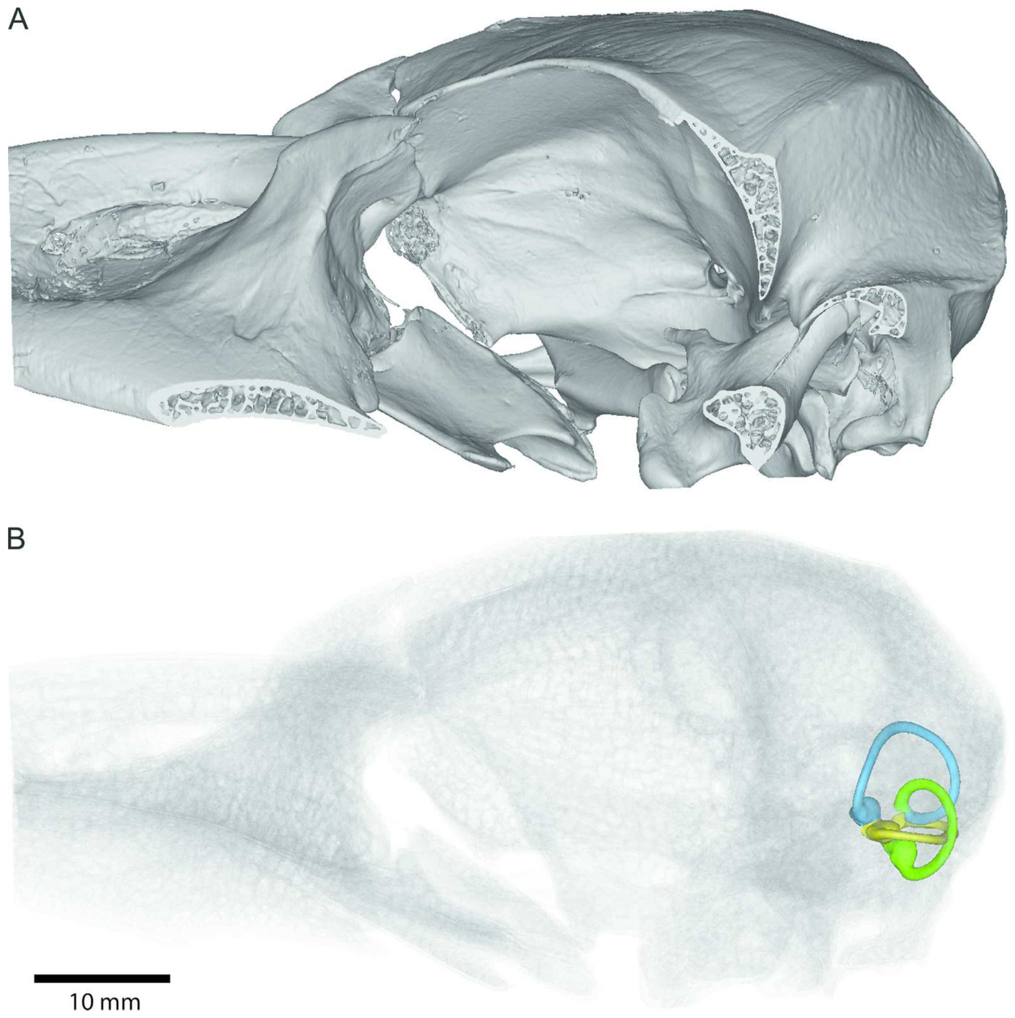

Fig. 1. Rendering of the skull of Podargus strigoides indicating the position of the endosseous semicircular canals. An opaque rendering is shown in (A), and a transparent rendering through which the endosseous canals (minus the vestibule and cochlear canal) are visible is shown in (B). Identity is indicated with colour for the anterior [=rostral] canal (blue), posterior [=caudal] canal (green), and lateral [=horizontal] canal (yellow). Scale bar: 10 mm.

140x140mm (300 x 300 DPI)

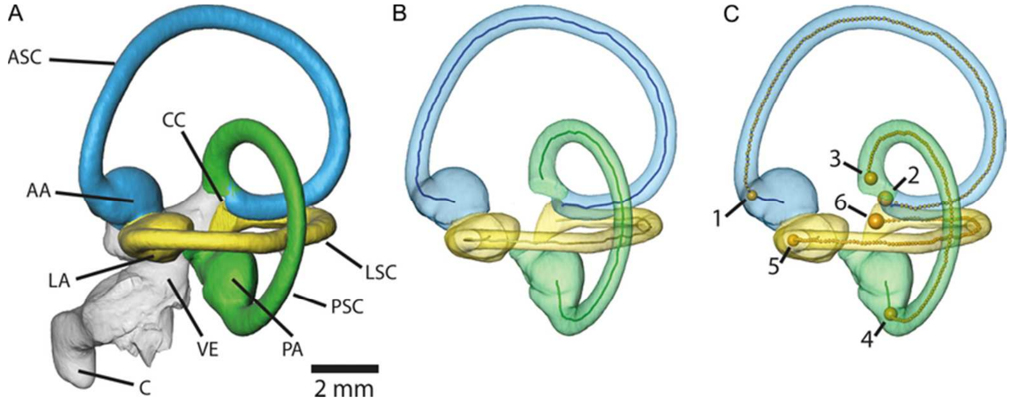

Fig. 2. Process of segmenting (A), skeletonising (B), and landmarking (C) the avian labyrinth. The four separate 3D voxel models are shown in grey (entire endosseous labyrinth), blue (anterior [=rostral] semicircular canal), green (posterior [=caudal] semicircular canal), and yellow (lateral [=horizontal] semicircular canal). Abbreviations: AA, ampulla of the anterior semicircular canal; ASC, anterior semicircular canal; C, cochlear duct; CC, crus communis; LA, ampulla of the lateral canal; LSC, lateral semicircular canal; PA, ampulla of the posterior semicircular canal; PSC, posterior semicircular canal; VE, vestibule. In panel (C), conventional landmarks at the ends of each semicircular canal are indicated by large yellow spheres and numbered 1–6. Sliding semilandmarks defining the course of each semicircular canal are indicated by small yellow spheres.

71x28mm (300 x 300 DPI)

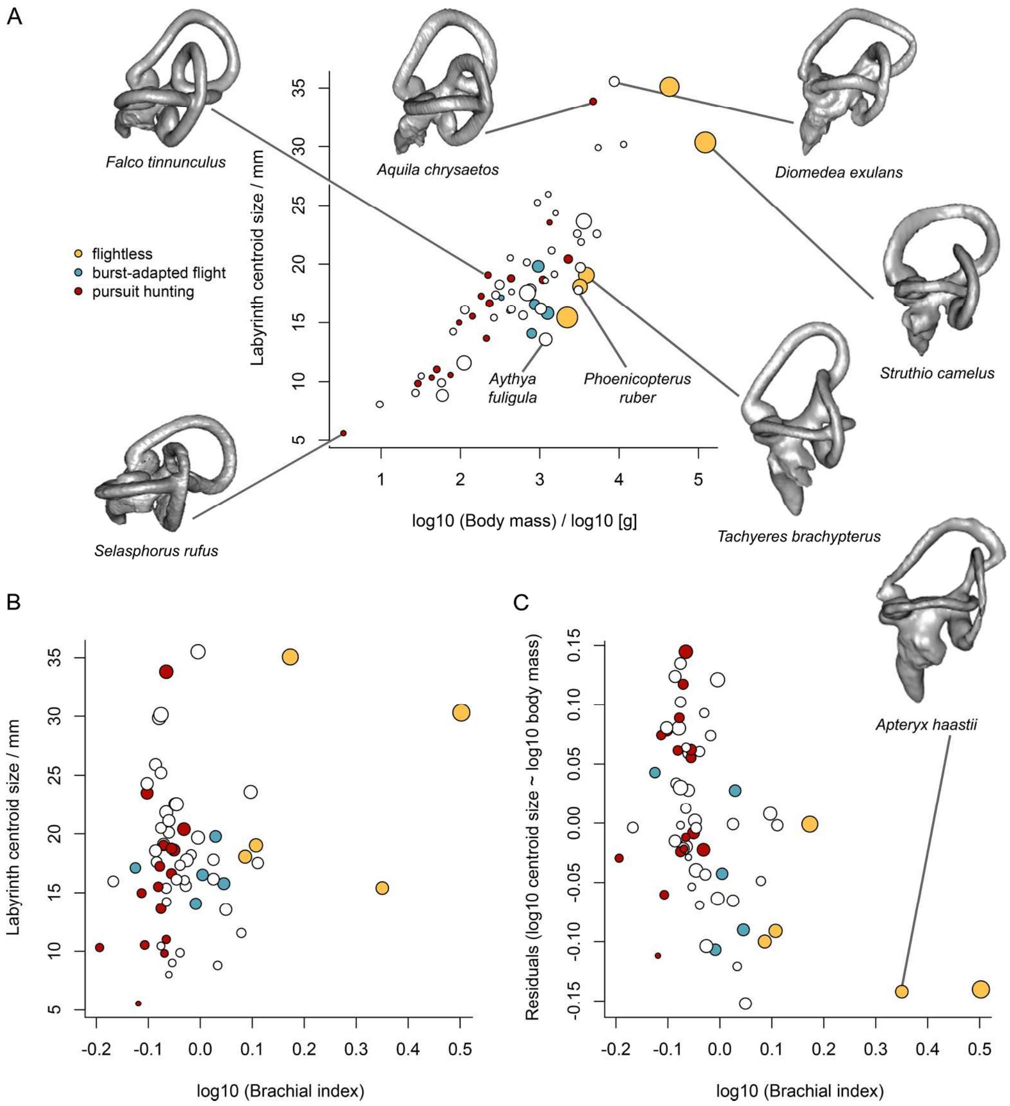

Fig. 3. Plots of (A) labyrinth centroid size on body mass, with point sizes scaled to brachial index (strong, multivariate relationship; Table 3), (B) labyrinth centroid size on brachial index (no relationship; Table 3), and (C) residuals of the relationship between labyrinth centroid size and body mass (Table 3, upper panel, model 2, variables log10-transformed) on brachial index. Points are coloured according to mutually exclusive subset categories in our multivariate flight categorisation for visualisation purposes only, and are white when none of these categories is present in a species. The decision as to which flight categories should be represented here was informed by the inferred significance of pursuit hunting for labyrinth morphology (see Results). Labyrinth models are shown in lateral view for selected taxa to illustrate the extremes of the relationship of labyrinth size with body mass.

199x218mm (300 x 300 DPI)

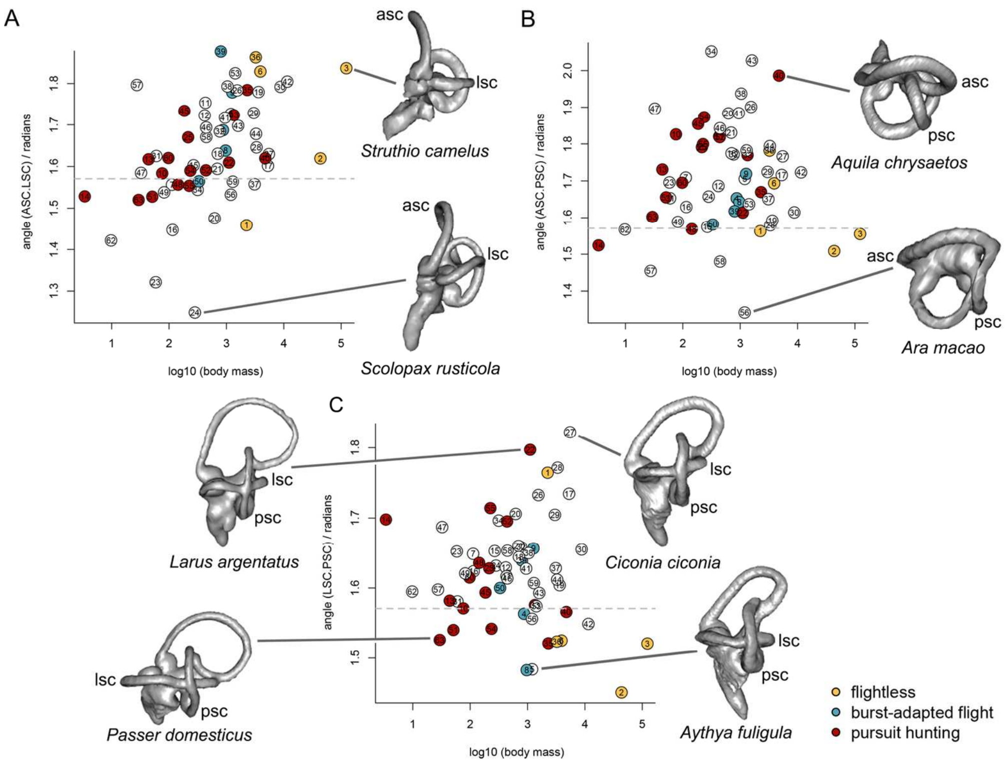

Figure 4. Plots of inter-canal angles versus body mass for the angles between (A) the anterior semicircular canal (ASC) and lateral semicircular canal (LSC), (B) the anterior and posterior semicircular canals (PSC), and (C) the lateral and posterior semicircular canals. Points are coloured according to a mutually exclusive subset categories in our multivariate flight categorisation for visualisation purposes only, and are white when none of these categories is present in a species. Labyrinth models are shown in anterior (A), dorsal (B) and lateral (C) views for selected taxa to illustrate the extremes of inter-canal angles among the sampled taxa.

137x103mm (300 x 300 DPI)

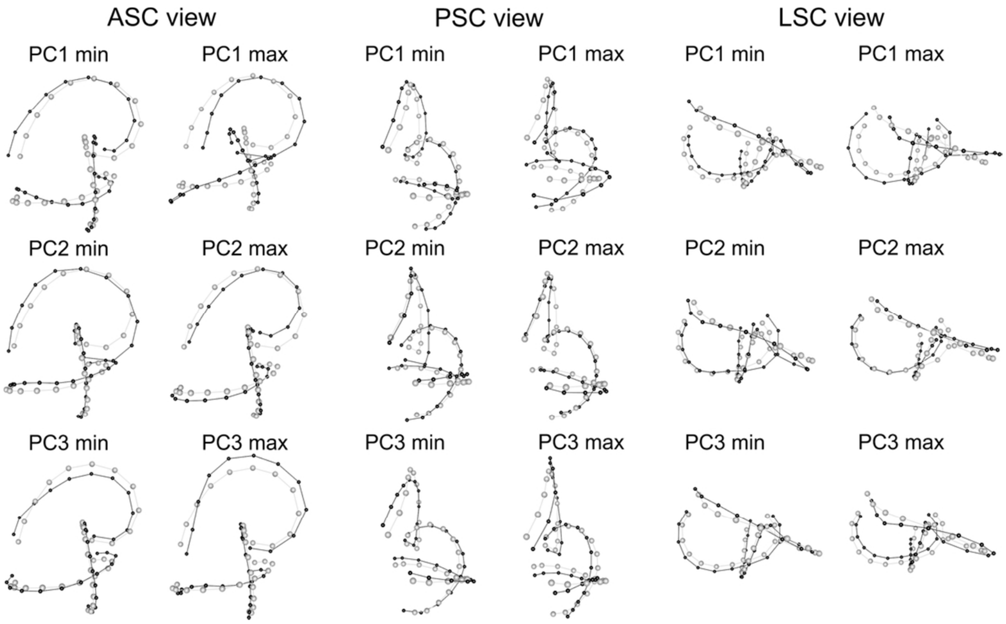

Fig. 5. Landmark configurations corresponding to the mean shape (grey symbols) and deformations along principal component axis PC1–PC3 (black symbols). Deformations correspond to the highest negative ('min') and positive ('max') score on each PC axis. Deformations are shown in three views corresponding approximately to the orthogonal planes of each of the three semicircular canals. Videos showing these deformations, and deformations of other PC axes (PC1–PC12) are available in the Supplementary Information.

102x63mm (300 x 300 DPI)

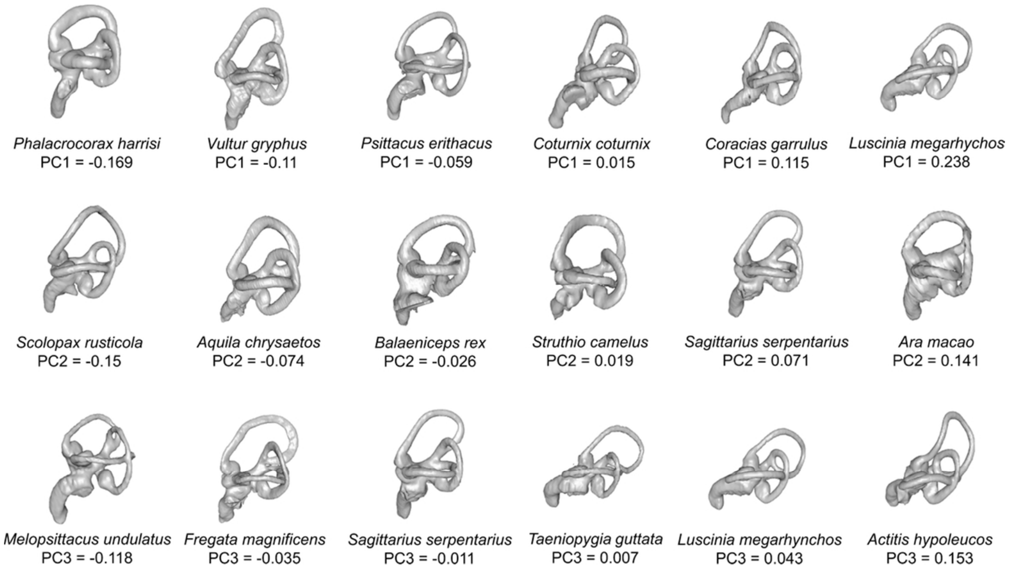

Phalacrocorax harrisi PC1 = -0.169
Vultur gryphus PC1 = -0.11
Psittacus erithacus PC1 = -0.059
Coturnix coturnix PC1 = 0.015
Coracias garrulus PC1 = 0.115
Luscinia megarhychos PC1 = 0.238

Scolopax rusticola PC2 = -0.15
Aquila chrysaetos PC2 = -0.074
Balaeniceps rex PC2 = -0.026
Struthio camelus PC2 = 0.019
Sagittarius serpentarius PC2 = 0.071
Ara macao PC2 = 0.141

Melopsittacus undulatus PC3 = -0.118
Fregata magnificens PC3 = -0.035
Sagittarius serpentarius PC3 = -0.011
Taeniopygia guttata PC3 = 0.007
Luscinia megarhynchos PC3 = 0.043
Actitis hypoleucos PC3 = 0.153

Fig. 6. 3D digital models of the endosseous labyrinths of selected species in lateral view, showing morphological changes among species distributed along PC1 (top row), PC2 (middle row) and PC3 (bottom row).

101x56mm (300 x 300 DPI)

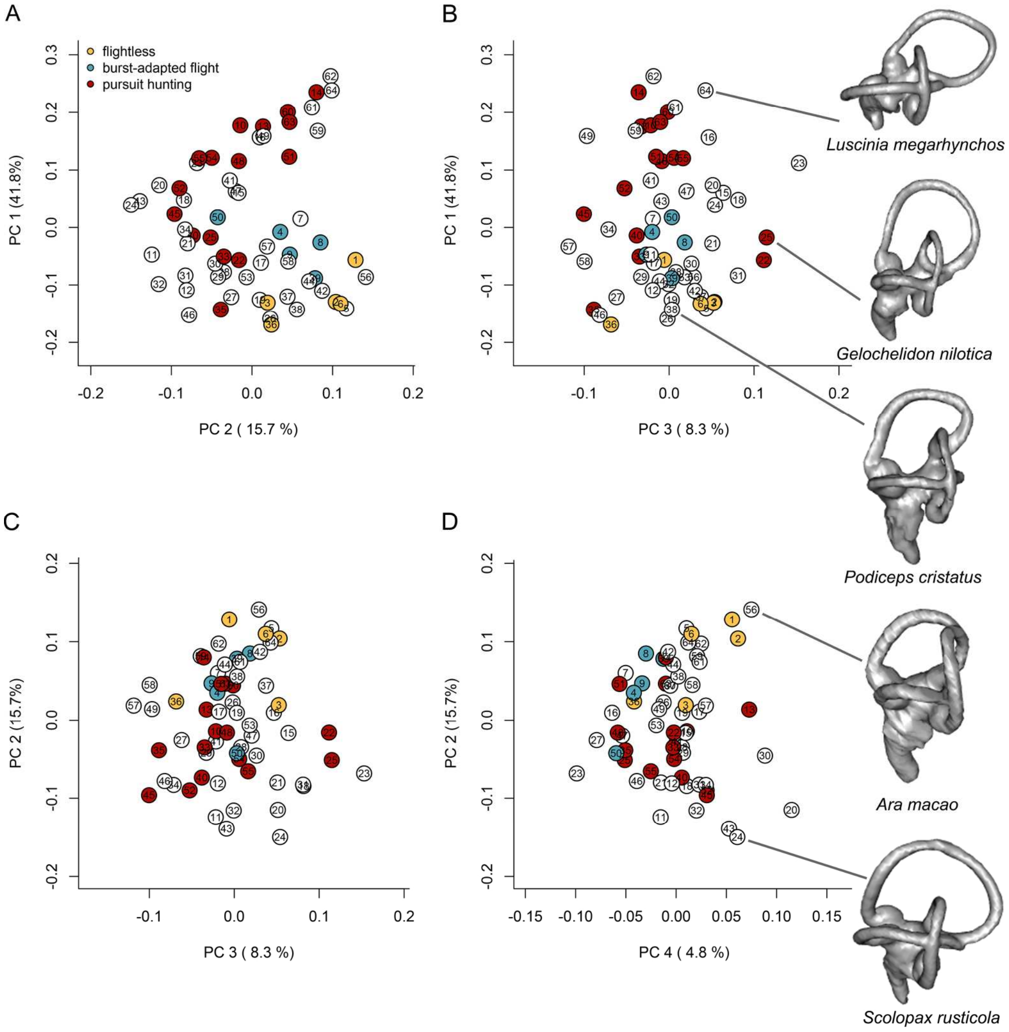

Fig. 7. Plots of principal component scores (A) PC1 versus PC2, and (B) PC1 versus PC3. The proportions of total shape variance explained by each axis are indicated in brackets (and see Table 4). Points are coloured according to three mutually exclusive categories in our multivariate flight categorisation, and greyed when none of these categories is present in a species. Numbers indicate taxa as denoted in Table 1. Labyrinth models of selected taxa are shown in lateral view to illustrate extreme values of PC1 and PC2.

187x191mm (300 x 300 DPI)

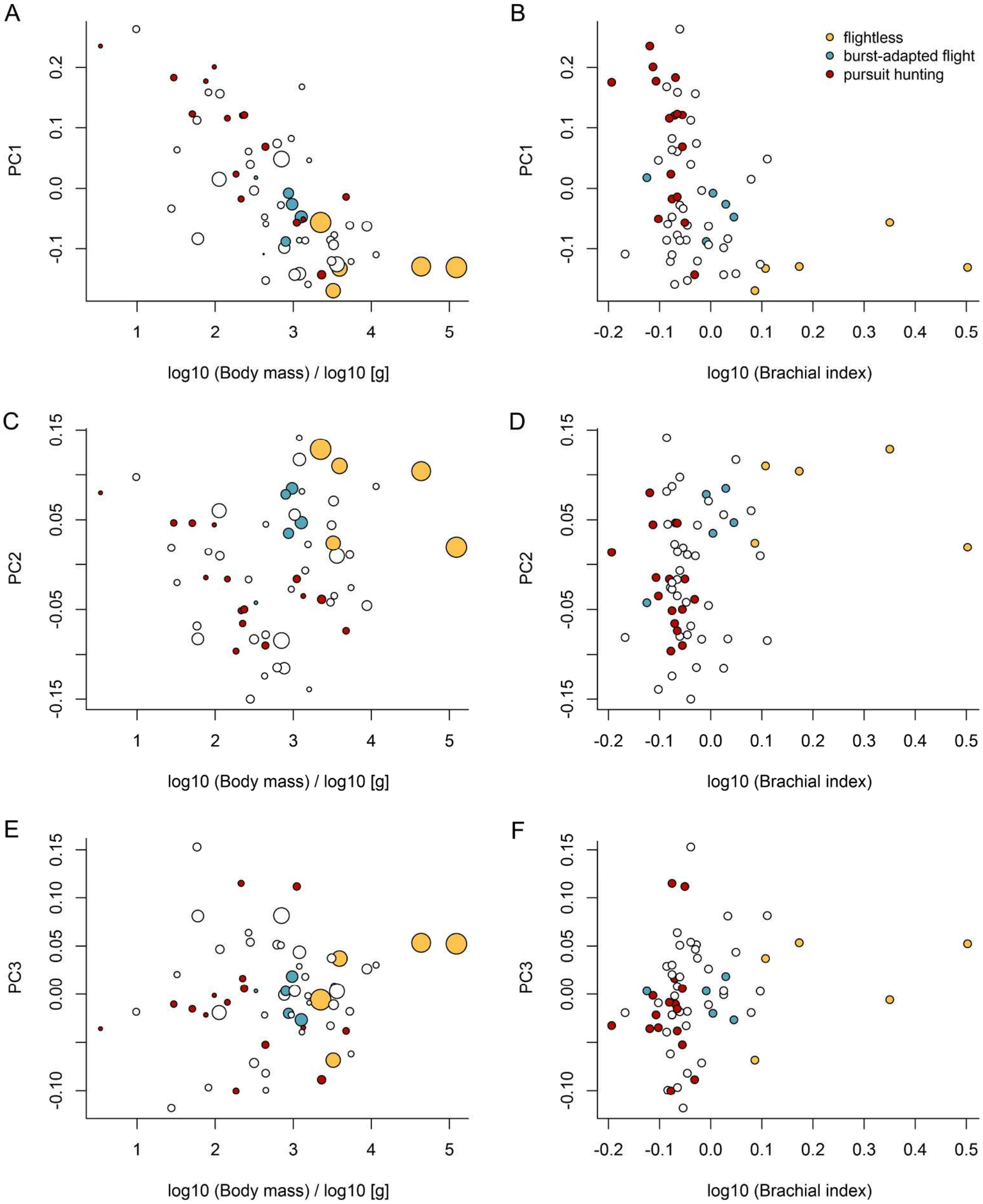

Fig. 8. Regressions of principal component axes 1–3 (PC1–PC3) on body mass (A,C,E) with point sizes scaled to brachial index, and on brachial index (B,D,F). PC1 shows a strongly significant relationship with body mass (A) (Table 6), but other axes shown here show no relationship with either body mass or brachial index (Tables 6–8). Points are coloured according to three mutually exclusive categories in our multivariate flight categorisation, and greyed when none of these categories is present in a species.

224x274mm (300 x 300 DPI)

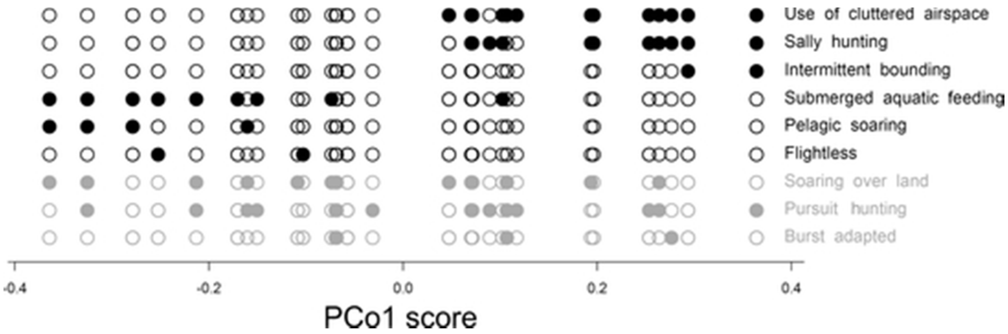

Fig. 9. Interpretation of principal coordinates axis 1 (PCo1) for flying style. The distribution of taxa scored as possessing each flying style (black discs) is shown along the first principal coordinates axis (PCo1; horizontal axis). Flight categories that show clustering towards either end of PCo1 are indicated in black, others are in grey.

46x14mm (300 x 300 DPI)

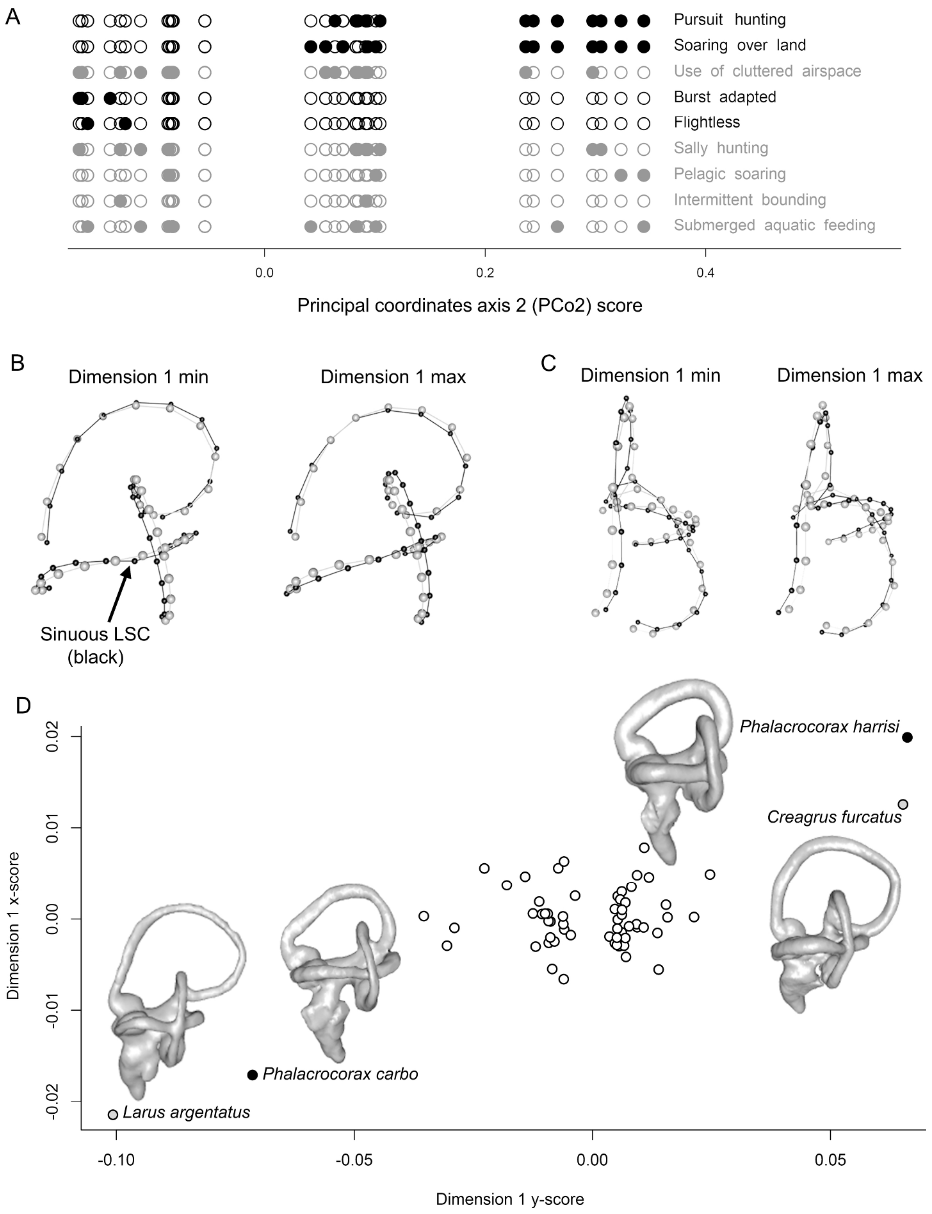

Fig. 10. Dimension 1 of our non-allometric two-block partial least squares (2B-PLS) analysis describes a multivariate association between a composite flying style variable (PCo2) and shape change in the labyrinth described by the principal components axes PC6, PC7, and PC11. (A) The distribution of taxa scored as possessing each flying style (black discs) is shown along the second principal coordinates axis (PCo2; horizontal axis). Flight categories that show clustering towards either end of PCo2 are indicated in black, others are in grey. (B–C) Labyrinth shape deformations (black symbols) implied by change of PC scores along dimension 1 seen in lateral (A) and anterior (B) views, as compared to the mean shape (grey symbols). Key shape differences are increasing sinuosity of the lateral canal and an increase in the angle between the planes of the anterior and posterior canals at negative shape scores on Dimension 1. (D) Ordination of taxa based on x and y scores of dimension 1 showing that two influential sister-taxon pairs act as influential datapoints in the analysis. The labyrinth models of these taxa are shown on the plot in lateral view.

224x288mm (300 x 300 DPI)

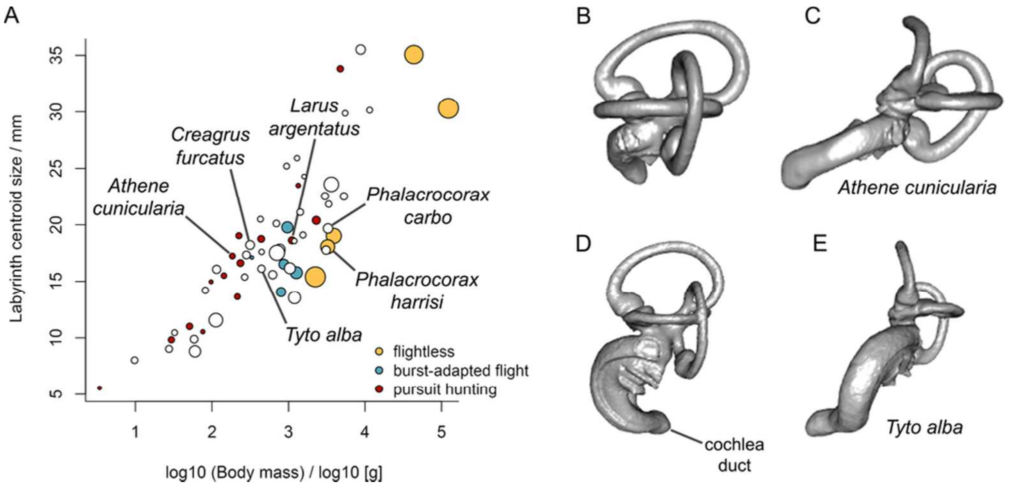

Fig. 11. Relationship between labyrinth centroid size and body mass (taken from Fig. 3A), with owls and outlier taxon pairs from 2B-PLS indicated. Tyto alba, the barn owl, has a proportionally reduced labyrinth and enlarged cochlea compared to Athene cunicularia, the burrowing owl. 3D virtual models of the labyrinths of A. cunicularia (B)–(C) and Tyto alba (D)–(E) are shown in lateral (B), (D), and anterior (C), (E) to illustrate this.

86x41mm (300 x 300 DPI)

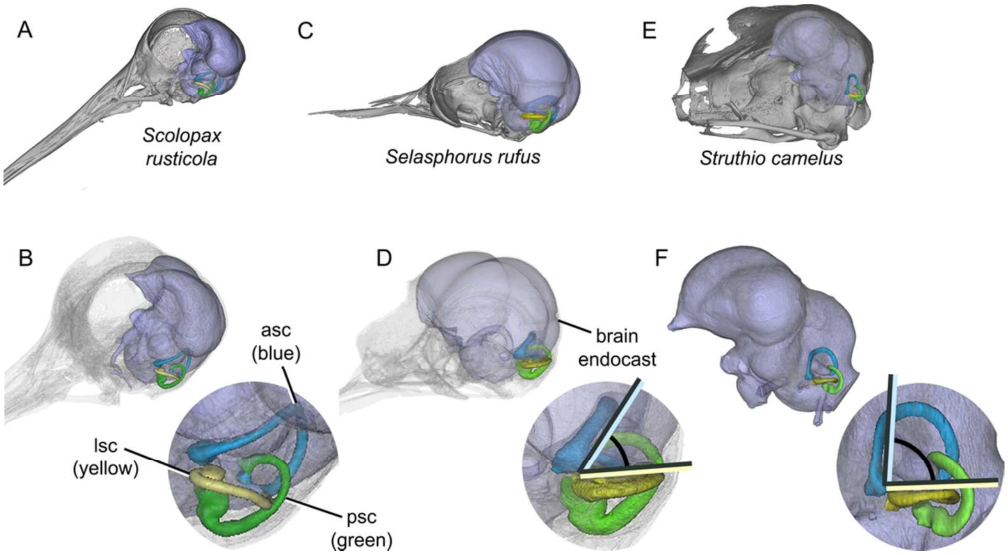

Fig. 12. Spatial constraints on the morphology of the avian semicircular canals, illustrated by 3D scan reconstruction models of (A)–(B), Scolopax rusticola the woodcock, (C)–(D), Selasphorus rufus, the rufous hummingbird, and (E)–(F), Stuthio camelus, the ostrich. (A), (C), and (E) show the endocast (purple) in context of the cranium (grey) in left lateral view. (B), (D), and (F) show closer images in anterolateral view with magnification of the semicircular canals. Scolopax rusticola and Selasphorus rufus show strong evidence of spatial deformation of the semicircular canals due to occupation of space by the brain, Struthio camelus does not. For example, the angle between the planes of the anterior and lateral canal is low in Scolopax rusticola and Selasphorus rufus (indicated) but close to orthogonal in Struthio camelus (indicated).

100x54mm (300 x 300 DPI)

Appendix S1. Discussion of flight categories.

Burst-adapted—Species that cannot undergo prolonged periods of steady level flight. Nevertheless, weak flight can be used in short bursts to escape predation or to reach roosting sites (Close and Rayfield, 2012).

Flightless—Species that are incapable of flight.

Flap-bounding—Intermittent flapping flight. Between episodes of flapping, species fold their wings tightly against the bod to streamline themselves during a non-flapping ballistic phase.

Pursuit hunting—Dynamic predators whose hunting techniques involve an extended chase in air, more reliant on maintaining high speeds than quick bursts of acceleration. Kleptoparasitism and piracy have similar requirements and are also included in this category. Fly catching is considered a form of pursuit hunting if the insects are both caught and eaten on the wing. Known as "continuous aerial hawking", this allows taxa to remain airborne for longer periods of time without the need for huge accelerations from a standing start. Both aerial and non-aerial targets are considered. For example, when hunting a fast-moving, agile target such as a swallow or a hare, a sustained tail-chase is required, the hunter matching the prey move for move until an opportunity arises to capture it.

Soaring over land—These species are able to exploit thermal updrafts in order to gain altitude with minimum energy expenditure. This character tends to be limited to larger non-passerine taxa with a strong but less agile flying ability.

Pelagic (dynamic) soaring—Thermals are considerably weaker over the open ocean than the continents, and are therefore not utilised during dynamic soaring. Instead, taxa take advantage of any wind shear existing above the sea surface between different layers of air, or updrafts occurring along the windward side of waves (Bruderer et al. (2010)).

Submerged aquatic feeding—Includes only those that are completely submerged underwater during feeding. Typically involves diving/plunging from a height or from the surface. Often propelled underwater using wings and/or feet, especially when in pursuit of prey.

Sally hunting—Dynamic species that attack prey from close range. Prey is pursued from a standing start (from the ground, a perch or a hover) and over a short distance. They are therefore characterised by a high accelerative ability. Both aerial and non-aerial targets can be sally hunted if they are capable of moving sufficiently quickly to escape predation – this is what warrants such high accelerations. Fly-catching is included if hunters are forced to return to a perch or the ground to eat, a position where a standing start is required for subsequent hunts. Often involves an element of surprise, sometimes necessary for the hunter to get to within close proximity of its prey.

Use of cluttered airspace—Species that inhabit environments with cluttered airspace. High degrees of manoeuvrability and slow flight are required to navigate through obstacles such as vegetation and rocks. This character was scored as absent when a species exclusively populates desert, open field, tundra, steppe, scree, moorland, lagoonal or pelagic environments, or if it soars over any clutter present (Taylor, 2014). Cliffs, estuaries, large inland water bodies (lakes and reservoirs), marshes, mudflats, rocky islands, saltpans and sandbanks were also considered to be sufficiently "uncluttered" herein to warrant a score of absent for this character. Statements such as "roosts in a tree" or "roosts under vegetation" were disregarded when scoring this character.

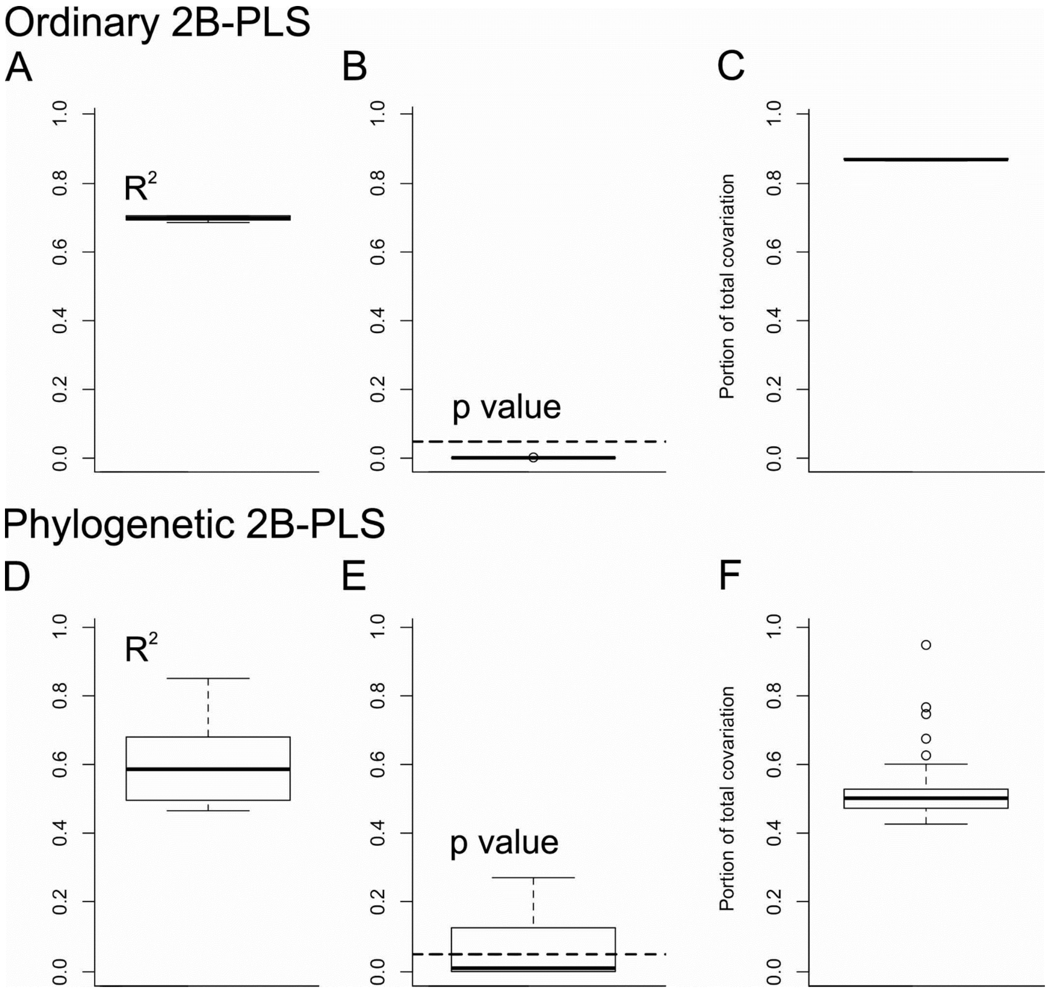

Fig. S1. Summary of ordinary (A–C) and phylogenetic (D–F; distribution of results over 100 phylogenies taken from Jetz et al., 2012; birdtree.org) 2B-PLS results comparing multivariate flight style to PC shape axes for endosseous labyrinth morphology including outliers and including all shape axes (PC1 [allometric shape change]–PC65). R^2 values shown in A and D; p values shown in panels B and E; proportion of total covariance explained by dimension 1 shown in panels C and F. The dashed horizontal line in B and E is the 0.05 threshold for statistical significance.

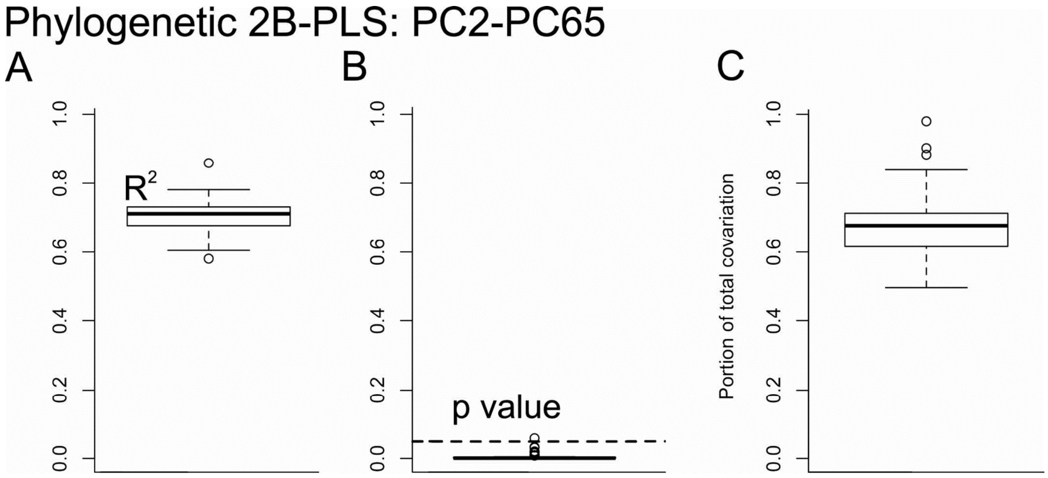

Fig. S2. Boxplots showing distributions of R^2 (A), p values (B), and portion of total covariance explained by dimension 1 (C) resulting from phylogenetic two-block partial least squares (2B-PLS) analyses excluding PC1 (i.e. non-allometric analysis), and conducted on a sample of 100 phylogenies taken from Jetz et al. (2012; birdtree.org), analysing all shape axes (PC1–PC65). The dashed horizontal line in B is the 0.05 threshold for statistical significance.

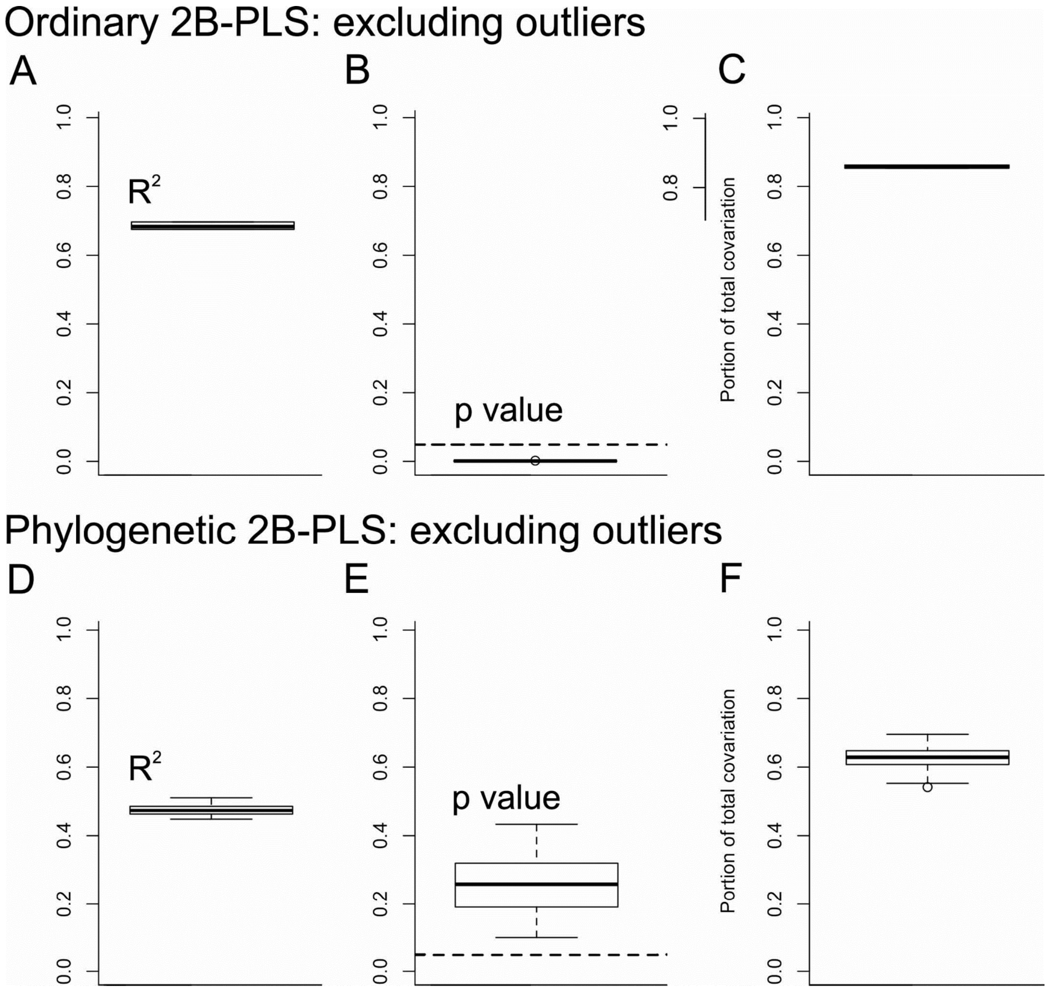

Ordinary 2B-PLS: excluding outliers

Phylogenetic 2B-PLS: excluding outliers

Fig. S3. Boxplots showing distributions of R^2 (A,D), p values (B,E), and portion of total covariance explained by dimension 1 (C,F) resulting from ordinary (A–C) and phylogenetic (D–F) two-block partial least squares (2B-PLS) analyses conducted on a sample of 100 phylogenies taken from Jetz et al. (2012; birdtree.org), analysing all shape axes (PC1–PC65). These analyses exclude the influential datapoints: *Larus argentatus* and *Creagrus furcatus*, and *Phalacrocorax harrisi* and *Phalacrocorax carbo*. The dashed horizontal line in B and E is the 0.05 threshold for statistical significance.

	Model	**λ**	**Variable**	**Coefficient**	**p-value**	**AICc**	**AICc-weight**	**R^2**
1**	angle(LSC, PSC) ~ log10(BI)	0.32	(Intercept)	1.61	<0.001	-130.2	0.90	-0.036
			log10(BI)	-0.07	0.496			
2*	angle(LSC, PSC) ~ log10(mass)	0.35	(Intercept)	1.62	<0.001	-125.7	0.09	-0.114
			log10(mass)	-0.01	0.591			
3	angle(LSC, PSC) ~ log10(BI) + log10(mass)	0.33	(Intercept)	1.62	<0.001	-121.3	0.01	-0.155
			log10(BI)	-0.06	0.626			
			log10(mass)	0	0.772			
1**	angle(ASC, PSC) ~ log10(BI)	0.83	(Intercept)	1.67	<0.001	-65.4	0.88	-0.019
			log10(BI)	-0.08	0.703			
2*	angle(ASC, PSC) ~ log10(mass)	0.84	(Intercept)	1.63	<0.001	-61	0.10	-0.093
			log10(mass)	0.01	0.613			
3	angle(ASC, PSC) ~ log10(BI) + log10(mass)	0.82	(Intercept)	1.63	<0.001	-57.9	0.02	-0.11
			log10(BI)	-0.12	0.577			
			log10(mass)	0.01	0.52			
1**	angle(ASC, LSC) ~ log10(mass)	0.85	(Intercept)	1.45	<0.001	-80.6	0.81	0.081
			log10(mass)	0.07	0.001*			
2*	angle(ASC, LSC) ~ log10(BI) + log10(mass)	0.88	(Intercept)	1.45	<0.001	-77	0.13	0.06
			log10(BI)	0.07	0.698			
			log10(mass)	0.07	0.001			
3	angle(ASC, LSC) ~ log10(BI)	0.99	(Intercept)	1.65	<0.001	-75.3	0.06	-0.002
			log10(BI)	0.22	0.242			

Table S1. Results of regressions of labyrinth inter-canal angles on $\log_{10}$ body mass and $\log_{10}$ brachial index (BI). Models are rank-ordered by AICc weight so the best model (**) is at the top. Models with similar AICc weights to the best model are indicated with **; and other models with non-negligible AICc weights (up to one-tenth with weight of the best model) are indicated with *. All variables are $\log_{10}$-transformed. N = 62 for all analyses in this table. R^2 is the generalised coefficient of determination described by Nagelkerke (1991), and negative values indicate that a model is worse than an intercept-only null model. Analyses we conducted across our sample of 100 phylogenies, yielding similar results each time. Only one such result is shown here.

	Model	λ	Variable	Coefficient	p-value	AICc	AICc-weight	R^2
1**	angle(LSC, PSC) ~ log10(BI)	0.39	(Intercept)	0.07	<0.001	-165.3	0.86	0.042
			log10(BI)	0.04	0.643			
2*	angle(LSC, PSC) ~ log10(mass)	0.34	(Intercept)	0.05	0.152	-161.7	0.14	-0.017
			log10(mass)	0.01	0.292			
3	angle(LSC, PSC) ~ log10(BI) + log10(mass)	0.35	(Intercept)	0.05	0.162	-156.5		
			log10(BI)	0.01	0.913			
			log10(mass)	0.01	0.365		0.00	-0.078
1**	angle(ASC, PSC) ~ log10(BI)	0.61	(Intercept)	0.13	0.005	-77.6	0.88	-0.014
			log10(BI)	-0.16	0.379			
2*	angle(ASC, PSC) ~ log10(mass)	0.67	(Intercept)	0.07	0.359	-73.1	0.09	-0.09
			log10(mass)	0.02	0.414			
3	angle(ASC, PSC) ~ log10(BI) + log10(mass)	0.54	(Intercept)	0.06	0.426	-70.9	0.03	-0.09
			log10(BI)	-0.25	0.192			
			log10(mass)	0.02	0.231			
1**	angle(ASC, LSC) ~ log10(BI)	0.72	(Intercept)	0.11	0.003	-115.1	0.95	0.042
			log10(BI)	0.3	0.029*			
2	angle(ASC, LSC) ~ log10(mass)	0.56	(Intercept)	0.05	0.376	-108.3	0.03	-0.069
			log10(mass)	0.02	0.093			
	angle(ASC, LSC) ~ log10(BI) + log10(mass)	0.69	(Intercept)	0.07	0.239	-107.4	0.02	-0.049
3			log10(BI)	0.26	0.071			
			log10(mass)	0.01	0.343			

Table S2. Results of regressions of positivised deviations of labyrinth inter-canal angles from 1.57 radians (= 90°) on $\log_{10}$ body mass and $\log_{10}$ brachial index (BI). Models are rank-ordered by AICc weight so the best model (**) is at the top. Models with similar AICc weights to the best model are indicated with **; and other models with non-negligible AICc weights (up to one-tenth with weight of the best model) are indicated with *. All variables are $\log_{10}$-transformed. N = 62 for all analyses in this table. R^2 is the generalised coefficient of determination described by Nagelkerke

(1991), and negative values indicate that a model is worse than an intercept-only null model. Analyses we conducted across our sample of 100 phylogenies, yielding similar results each time. Only one such result is shown here.

	Model	λ	Variable	Coefficient	p-value	AICc	AICc-weight	R^2
1**	summed deviations from 90° ~ log10(BI)	0.88	(Intercept)	0.3	<0.001	-56.2	0.67	-0.007
			log10(BI)	0.19	0.394			
2*	summed deviations from 90° ~ log10(mass)	0.79	(Intercept)	0.18	0.06	-54.4	0.27	-0.036
			log10(mass)	0.04	0.061			
3	summed deviations from 90° ~ log10(BI) + log10(mass)	0.82	(Intercept)	0.18	0.061	-51.2	0.06	-0.054
			log10(BI)	0.08	0.735			
			log10(mass)	0.04	0.093			

Table S3. Results of regressions of summed positivised deviations of labyrinth inter-canal angles from 1.57 radians (= 90°) on $\log_{10}$ body mass and $\log_{10}$ brachial index (BI). Models are rank-ordered by AICc weight so the best model (**) is at the top. Models with similar AICc weights to the best model are indicated with **; and other models with non-negligible AICc weights (up to one-tenth with weight of the best model) are indicated with *. All variables are $\log_{10}$-transformed. N = 62 for all analyses in this table. R^2 is the generalised coefficient of determination described by Nagelkerke (1991), and negative values indicate that a model is worse than an intercept-only null model. Analyses we conducted across our sample of 100 phylogenies, yielding similar results each time. Only one such result is shown here.

	Model	**λ**	**Variable**	**Coefficient**	**p-value**	**AICc**	**AICc weight**	**R^2**
1	PC 4 ~ log10(BI)	0.81	(Intercept)	0	0.886	-203.5	0.52	-0.05
			log10(BI)	0.05	0.443			
2	PC 4 ~ log10(BI) + log10(mass)	1.18	(Intercept)	-0.05	0.048	-202.3	0.29	-0.03
			log10(BI)	-0.02	0.605			
			log10(mass)	0.01	0.001			
3	PC 4 ~ log10(mass)	1.04	(Intercept)	-0.05	0.139	-201.5	0.19	-0.08
			log10(mass)	0.01	0.038			

Table S4. Results of regressions of labyrinth fourth principal component (PC4) axis on body mass and brachial index. Models are rank-ordered by AICc weight so the best non-null model is at the top. However, all models have worse AICc values than an intercept-only null model, indicated by negative values of R^2. All variables are $\log_{10}$-transformed. N = 62 for all analyses in this table. R^2 is the generalised coefficient of determination described by Nagelkerke (1991), and negative values indicate that a model is worse than an intercept-only null model.

	Model	**λ**	**Variable**	**Coefficient**	**p-value**	**AICc**	**AICc weight**	**R^2**
1	PC 5 ~ log10(BI)	1.02	(Intercept)	0	0.929	-218.7	0.95	0.01
			log10(BI)	-0.12	0.043			
2	PC 5 ~ log10(mass)	1.02	(Intercept)	-0.03	0.239	-211.7	0.03	-0.12
			log10(mass)	0.01	0.222			
3	PC 5 ~ log10(BI) + log10(mass)	1.01	(Intercept)	-0.03	0.2	-211.2	0.02	-0.08
			log10(BI)	-0.14	0.018			
			log10(mass)	0.01	0.084			

Table S5. Results of regressions of labyrinth fifth principal component (PC5) axis on body mass and brachial index. Models are rank-ordered by AICc weight so the best non-null model is at the top. However, all models have AICc values that are similar to or worse than an intercept-only null model, indicated by low or negative values of R^2. All variables are $\log_{10}$-transformed. N = 62 for all analyses in this table. R^2 is the generalised coefficient of determination described by Nagelkerke (1991), and negative values indicate that a model is worse than an intercept-only null model.

	Model	**λ**	**Variable**	**Coefficient**	**p-value**	**AICc**	**AICc weight**	**R^2**
1	PC 6 ~ log10(BI)	0.84	(Intercept)	-0.01	0.487	-234.6	0.96	-0.01
			log10(BI)	0.1	0.057			
2	PC 6 ~ log10(mass)	0.84	(Intercept)	-0.03	0.243	-228.1	0.04	-0.12
			log10(mass)	0.01	0.208			
3	PC 6 ~ log10(BI) + log10(mass)	0.85	(Intercept)	-0.02	0.288	-224.5	0.01	-0.14
			log10(BI)	0.09	0.102			
			log10(mass)	0	0.419			

Table S6. Results of regressions of labyrinth sixth principal component (PC6) axis on body mass and brachial index. Models are rank-ordered by AICc weight so the best non-null model is at the top. However, all models have AICc values that are worse than an intercept-only null model, indicated by negative values of R^2. All variables are $\log_{10}$-transformed. N = 62 for all analyses in this table. R^2 is the generalised coefficient of determination described by Nagelkerke (1991), and negative values indicate that a model is worse than an intercept-only null model.

	Model	λ	Variable	Coefficient	p-value	AICc	AICc weight	R^2
1	PC 7 ~ log10(BI)	0.59	(Intercept)	0	0.877	-226.0	0.93	-0.05
			log10(BI)	0.05	0.332			
2	PC 7 ~ log10(mass)	0.53	(Intercept)	0	0.936	-220.7	0.07	-0.15
			log10(mass)	0	0.944			
3	PC 7 ~ log10(BI) + log10(mass)	0.59	(Intercept)	0	0.821	-215.6	0.01	-0.20
			log10(BI)	0.06	0.303			
			log10(mass)	0	0.699			

Table S7. Results of regressions of labyrinth seventh principal component (PC7) axis on body mass and brachial index. Models are rank-ordered by AICc weight so the best non-null model is at the top. However, all models have AICc values that are worse than an intercept-only null model, indicated by negative values of R^2. All variables are $\log_{10}$-transformed. N = 62 for all analyses in this table. R^2 is the generalised coefficient of determination described by Nagelkerke (1991), and negative values indicate that a model is worse than an intercept-only null model.

	Model	**λ**	**Variable**	**Coefficient**	**p-value**	**AICc**	**AICc weight**	**R^2**
1	PC 8 ~ log10(mass)	0.74	(Intercept)	0.03	0.114	-232.1	0.56	-0.05
			log10(mass)	-0.01	0.01			
5	PC 8 ~ log10(BI)	0.49	(Intercept)	-0.01	0.369	-231.1	0.34	-0.07
			log10(BI)	0.03	0.532			
6	PC 8 ~ log10(BI) + log10(mass)	0.77	(Intercept)	0.04	0.075	-228.8	0.11	-0.07
			log10(BI)	0.09	0.082			
			log10(mass)	-0.02	0.003			

Table S8. Results of regressions of labyrinth eighth principal component (PC8) axis on body mass and brachial index. Models are rank-ordered by AICc weight so the best non-null model is at the top. However, all models have AICc values that are worse than an intercept-only null model, indicated by negative values of R^2. All variables are $\log_{10}$-transformed. N = 62 for all analyses in this table. R^2 is the generalised coefficient of determination described by Nagelkerke (1991), and negative values indicate that a model is worse than an intercept-only null model.